國　立　交　通　大　學

電子物理學系

碩士論文

$Bi_{2-x}Pb_xSr_zCo_2O_y$ 和$(Bi_{0.25}Sb_{0.75})_2(Se_{2.35}Te_{0.65})$的核磁共振研究

NMR Study of $Bi_{2-x}Pb_xSr_zCo_2O_y$ 和$(Bi_{0.25}Sb_{0.75})_2(Se_{2.35}Te_{0.65})$

研 究 生 ：黃筧

指導教授 ：楊本立 教授

中華民國一百零一年七月

國立交通大學電子物理學系碩士班

學生：黃筧　　指導教授:楊本立 教授

中文摘要

本論文主要是利用核磁共振(NMR)的技術來探討磁性材料 $Bi_{2-x}Pb_xSr_zCo_2O_y$(x=0-0.61, y=8.47-8.62, z=1.78-1.99)在不同的 Pb 濃度中的磁性變化以及拓譜絕緣體$(Bi_{0.25}Sb_{0.75})_2(Se_{2.35}Te_{0.65})$的特殊電子結構。首先,我們發現$Bi_{2-x}Pb_xSr_zCo_2O_y$的磁性會隨Pb的濃度而改變，且室溫的磁化率隨 Pb 的加入而急速上升。我們量測樣品中的 ^{59}Co 的 NMR 頻率位移在不同溫度下的變化，發現此磁化率上升與含鉛樣品中 Co^{4+}的軌道磁化率增加有關。

拓譜絕緣體是一種具有特殊表面態的材料，根據理論，這種表面態並不會因為晶格缺陷或排列錯亂而被破壞。樣品$(Bi_{0.25}Sb_{0.75})_2(Se_{2.35}Te_{0.65})$是已知的拓譜絕緣體材料 Bi_2Se_3 摻雜了 Sb 和 Te 兩個元素所產生的，且仍具有拓譜表面態。我們發現這些摻雜是均勻分布在 Bi_2Se_3 的結構中，確認了所出現的表面態的確是樣品整體所出現的結果，而不是由局部 Bi_2Se_3 所造成的。

Department of Electrophysics

National Chiao Tung University

Student: Jian Huang Advisors: Prof. Ben-Li Young

Abstract

The electronic band structure of topological insulator and layered cobalt oxides structure all have attracted much attention, because their unusual physical properties. The topological insulator is a material which has an insulating bulk state and gapless surface states. The electronic structure of Co ion in the layered cobalt oxides structure which have two splitted t_{2g} and e_g orbitals originated from 5-degenerate 3*d*-orbital. This thesis reports Nuclear Magnetic Resonance (NMR) study of the topological insulator $(Bi_{0.25}Sb_{0.75})_2$ $(Se_{2.35}Te_{0.65})$ and the layered cobalt oxides compounds $Bi_{2-x}Pb_xSr_zCo_2O_y$ (x=0-0.61, y=8.47-8.62, z=1.78-1.99).

We measured the ^{209}Bi and ^{121}Sb NMR spectra in $(Bi_{0.25}Sb_{0.75})_2$ $(Se_{2.35}Te_{0.65})$ single crystal. We found that the ^{209}Bi NMR spectra of $(Bi_{0.25}Sb_{0.75})_2(Se_{2.35}Te_{0.65})$ is extraordinary broader than the ^{209}Bi NMR spectra of Bi_2Se_3, suggesting that the Bi atoms are randomly distribution in the crystal. The spin-spin relaxation time (T_2) of ^{209}Bi and ^{121}Sb are all show two T_2 components, it means that the both atoms are bonding with Se and Te two atoms. According to our experimental results, the $(Bi_{0.25}Sb_{0.75})_2$ $(Se_{2.35}Te_{0.65})$ has strong lattice distortion than Bi_2Se_3.

We measured the ^{59}Co NMR spectra in three different chemical compositions $Bi_{2-x}Pb_xSr_zCo_2O_y$ single crystal with different temperatures. The two different charge states of Co^{3+} and Co^{4+} peak are clearly showed in ^{59}Co NMR spectra, and the Pb doping increases the Co^{4+} peak intensity. We also measured Co^{3+} NMR frequency shift as a function of temperature for the three different samples. We found that the Co^{3+} NMR frequency shift at high temperature range (T>100K) is similarity in three different

samples, it means that the local susceptibility of Co^{3+} ions is same at three samples.

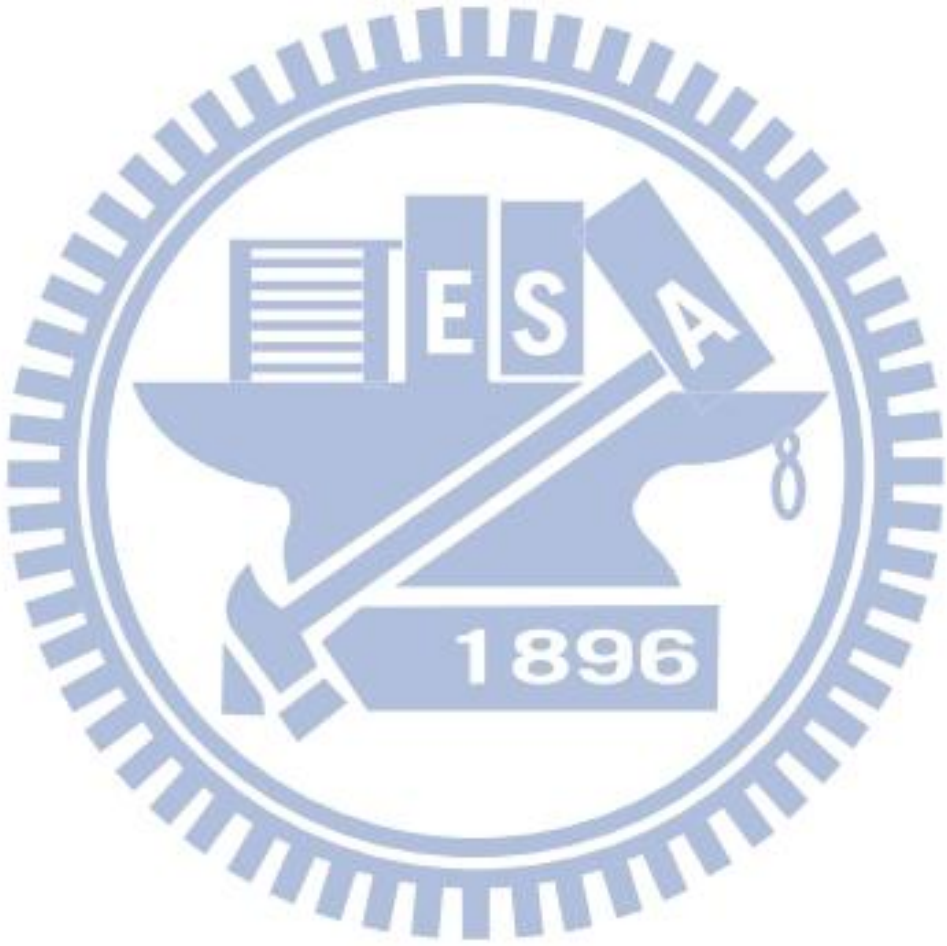

致謝

兩年一下就過去了，首先我要感謝我的父母，因為他們我才有機會就讀研究所。另外還要感謝我的指導老師楊本立教授在這兩年的指導，使我學到 NMR 的原理。在實驗室裡面，感謝學長朱培元的幫助，他除了在學業上面給予我許多的教導，在生活上也給了我許多的支援，並且對於實驗室的維護也花了許多時間和精力，還有我的同學源龍，也在我的實驗上面給予我與多幫忙。最後，我要感謝我的朋友們，讓我在這煩悶的研究生生活增添許多歡熱，讓我可以度過這兩年。

目錄

Chapter 1 introduction

The electronic band structure is a very importation topic in the solid state physics, because we can use this concept to explanation many physical phenomena like: magnetic materials, thermoelectric materials and topological insulator etc. In this thesis, we study the magnetic material $Bi_{2-x}Pb_xSr_zCo_2O_y$ and topological insulator $(Bi_{0.25}Sb_{0.75})_2(Se_{2.35}Te_{0.65})$ two materials. We want to find out the electronic band structure how to affect physical phenomena.

1-1 Brief introduction to $Bi_{2-x}Pb_xSr_zCo_2O_y$

Since the discovery of large thermoelectric power material in layered cobalt oxides $NaCo_2O_4$ [1], layered cobalt oxides have been immediately investigated and several new layered cobalt oxides compounds have been found, like: $Ca_3Co_4O_9$ and $Bi_2Sr_2Co_2O_X$ [2-4]. In addition, superconductivity has been observed in $Na_{0.35}CoO_2{\cdot}1.3H_2O$ [5]. It is also found that $Na_{0.68}CoO_2$ has a magnetic transition at 22K [6], and (Bi,Pb)-Sr-Co-O is ferromagnetic below T_C=3.2K[7]. Thus, it seems that this layered cobalt oxides plays an important role in the above physical properties. Theoretical and experimental studies suggest that the large thermoelectric power in layered cobalt oxides is caused by the degeracy of the 3d electronic orbitals of Co ions [8-12].

Recently, it has been found that the $Bi_{2-x}Pb_xSr_zCo_2O_y$ compound has a misfit-layered structure with a two-dimensional CoO_2 triangular lattice (see Fig.1-1) [13]. The electronic state of Co ions is mixed by Co^{3+} and Co^{4+} two states [11], and both Co^{3+} and Co^{4+} are in the low spin state [9]. The Co^{4+}/Co^{3+} ratio in this material can be adjusted by the hole doping [11]. Actually, the magnetic properties of $Bi_{2-x}Pb_xSr_zCo_2O_y$ compound depend on the Co^{4+}/Co^{3+} ratio [9, 11]. Therefore, the $Bi_{2-x}Pb_xSr_zCo_2O_y$ compound would give an opportunity to study the magnetic properties in the layered cobalt oxides structure.

In this thesis, we using the NMR techniques to measurement the three different chemical compositions of $Bi_{2-x}Pb_xSr_zCo_2O_y$ (see Table. I). These samples are all show different Co^{4+}/Co^{3+} ratio and different magnetic susceptibility (see Fig.3-1). Therefore, we can use the NMR measured results to find out the relationship between the Co^{4+}/Co^{3+} ratio and magnetic properties.

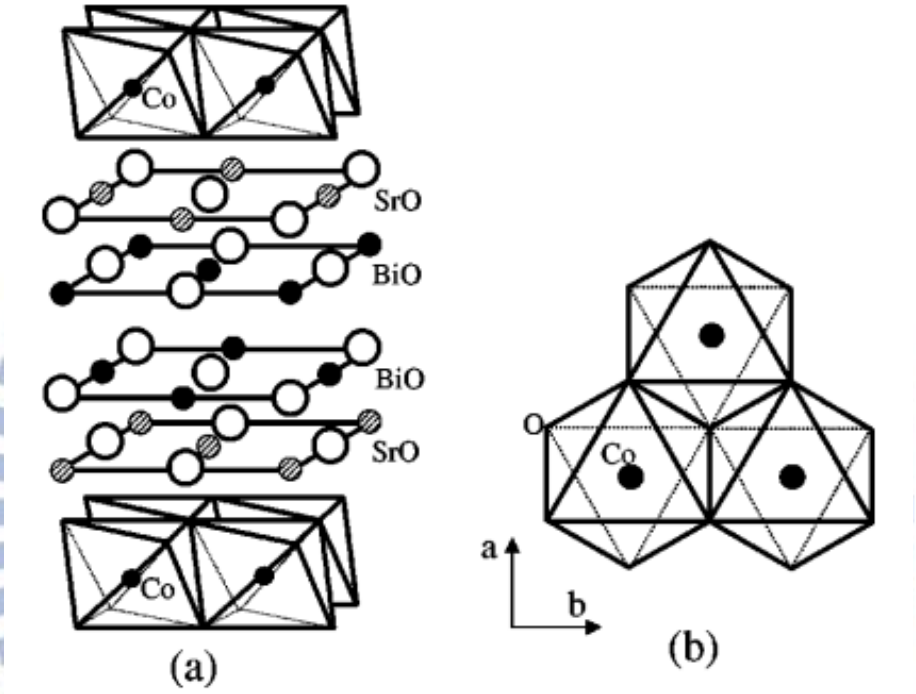

Fig.1-1 (a) Crystal structure of $Bi_{2-x}Pb_xSr_zCo_2O_y$ (b) top view for cobalt oxide layer [11]

Sample	Bi	Pb	Sr	Co	O	Co^{3+}:Co^{4+}
A	2.04	0.00	1.99	2.00	8.47	1.16:0.84
B	1.55	0.61	1.99	2.00	8.52	0.81:1.19
C	1.65	0.55	1.78	2.00	8.62	0.36:1.64

Table 1 Chemical compositions of $Bi_{2-x}Pb_xSr_zCo_2O_y$.

1-2 Brief introduction to $(Bi_{0.25}Sb_{0.75})_2(Se_{2.35}Te_{0.65})$

The topological insulator is a new state of material that shows many interesting physics phenomena and technological applications, such as spintronics devices [14]. The characterized of three-dimensional topological insulator is a material which has an insulating bulk state and gapless surface Dirac cone state [15]. The first 3D topological insulator is the semiconducting alloy $Bi_{1-x}Sb_x$, which unusual surface states band were measured in an angle resolved photoemission spectroscopy (ARPES) experiment by a Princeton University group led by Hasan in 2008 [17], and this semiconducting alloy exist a strength spin-orbital coupling. In 2009, other topological insulator materials Bi_2Se_3, Bi_2Te_3 and Sb_2Te_3, was been found [18]. The topological insulator Bi_2Se_3 electronic band structure schematic diagram is shows in Fig.1-2. The black line is represented bulk states, which has a band gap between conduction band and valence band. It means that the bulk state is an insulating state. The green line is represented surface state, which shows gapless surface Dirac cone. It means that the surface state is a conduction states. The conducting surface state of topological insulator will not disappear due to lattice distortion as long as time reversal symmetry is not broken [16].

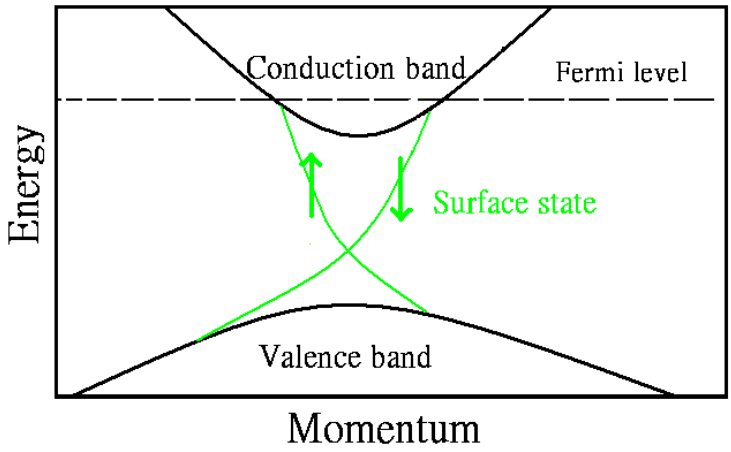

Fig.1-2 The topological insulator Bi_2Se_3 electronic band structure schematic diagram. The black line is represented bulk state, and the green line is represented surface state.

Our experiment is study the $(Bi_{0.25}Sb_{0.75})_2(Se_{2.35}Te_{0.65})$, which has been reported a good thermoelectric alloy [22, 23] and Topological Insulator [24, 25]. Basic structure unit of $(Bi_{0.25}Sb_{0.75})_2(Se_{2.35}Te_{0.65})$ is same as Bi_2Se_3 shows in Fig.1-3. The Se in the layer (1) and layer (5) are prone to vacancy creations, which is suppressed by Te doping. In the other hand the Sb atoms are into the Bi positions. According to ARPES measurement, the $(Bi_{0.25}Sb_{0.75})_2(Se_{2.35}Te_{0.65})$ has an unusually surface state like Topological Insulator (see Fig.1-4). As we know, the doping will produce the strong lattice distortion, but this lattice distortion seen not make surface state disappear. However, we can't sure the ARPES measurement result is form $(Bi_{0.25}Sb_{0.75})_2(Se_{2.35}Te_{0.65})$ or some defect cluster are Bi_2Se_3 in $(Bi_{0.25}Sb_{0.75})_2(Se_{2.35}Te_{0.65})$. If we can solve this problem, it will help the development of novel devices based on topological insulators [14].

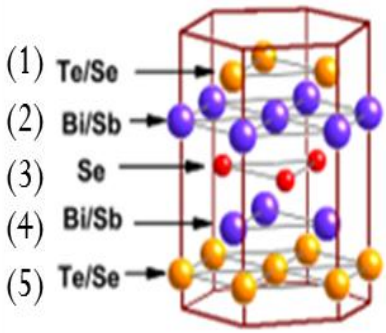

Fig.1-3 Basic structure unit of $(Bi_{0.25}Sb_{0.75})_2(Se_{2.35}Te_{0.65})$ [24]

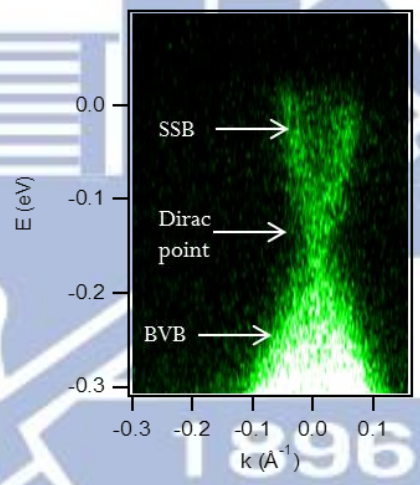

Fig.1-4 ARPES of $(Bi_{0.25}Sb_{0.75})_2(Se_{2.35}Te_{0.65})$

Chapter 2 The basic theory of NMR

NMR is a resonance phenomenon for the nuclei absorbing and re-emitting electromagnetic radiation in a static magnetic field. This electromagnetic radiation has specific resonance frequency which depends on the strength of the static magnetic field, and the environment of the nuclear site. Therefore, the NMR techniques is an important tool to probe the structure and the magnetic and electronic properties on an atomic scale.

2-1 Zeeman effect

NMR is based on the interaction of a nucleus with a uniform external magnetic field. This phenomenon is known as the Zeeman effect.

The Hamiltonian H for a nucleus having nuclear spin I in a static field $B=B_0\hat{\mathbf{z}}$ is

$$\widehat{\boldsymbol{H}} = -\boldsymbol{\gamma}\hbar\widehat{\boldsymbol{I}_z}\boldsymbol{B_0} \quad (2.1)$$

,where I_z is z component of nuclear spin operator, γ is gyromagnetic ratio, and $\hbar$ is Planck constant.

The eigenvalues are

$$E_{I,m} = -\gamma\hbar B_0 m \quad (2.2)$$

where m is the quantum number, m=I, I-1, I-2 , … ,-I. The degeneracy of the nuclear spin, removed by a magnetic field, is called Zeeman effect.

For a spin of $I=\frac{1}{2}$, $m = \pm\frac{1}{2}$ so there are two eigenstates with energies $E_{\frac{1}{2},\pm\frac{1}{2}} = \mp\frac{1}{2}\gamma\hbar B_0$ (Fig.2-1).

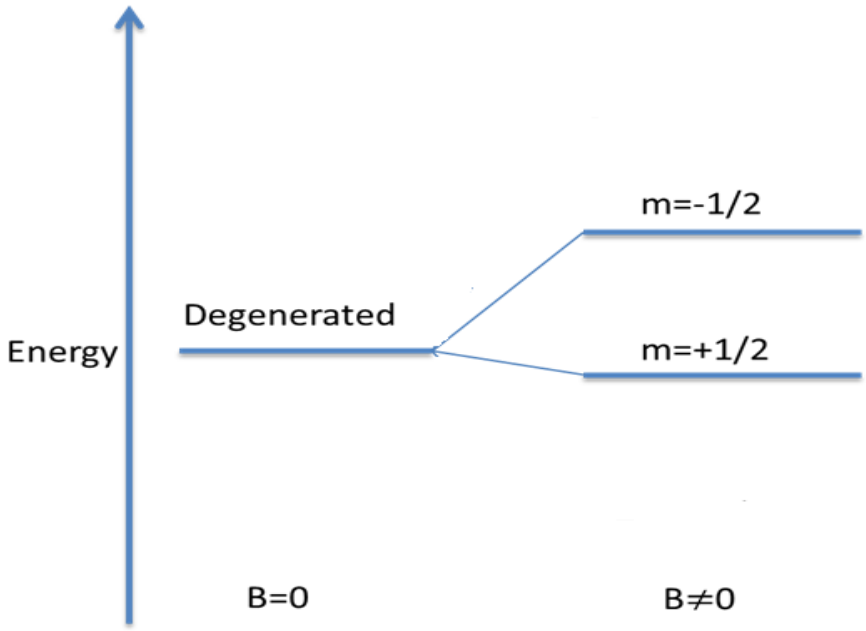

(a) (b)

Fig.2-1 (a)The nuclei energy levels without magnetic field , (b) and with magnetic field.

2-2 The NMR signal

In a quantum mechanical formalism, the excitation of the nuclear state by electromagnetic waves can be described as a resonant absorption of photon. The energy of an absorbed photon is $\mathrm{E} = \hbar\omega_0$, where ω_0 is the resonance frequency. According to the selection rules, the nuclear states transitions is $\Delta\,\mathrm{m} = \pm 1$. So, allowed transitions energy $\Delta\,\mathrm{E}$ between the nuclei states is $\gamma\hbar B_0$. Therefore, a magnetic resonance absorption will only occur when $\Delta\,\mathrm{E} = \hbar\omega_0 = \gamma\hbar B_0$. The excitation is usually in the radio frequency (rf) regime.

In a classical description, we used the Bloch equation to description magnetization motion.

The Bloch equation is

$$\frac{d}{dt}\begin{bmatrix} M_x \\ M_y \\ M_z \end{bmatrix} = \gamma \begin{bmatrix} i & j & k \\ M_x & M_y & M_z \\ B_x & B_y & B_z \end{bmatrix} - \begin{bmatrix} 1/T_2 & 0 & 0 \\ 0 & 1/T_2 & 0 \\ 0 & 0 & 1/T_1 \end{bmatrix} \begin{bmatrix} M_x \\ M_y \\ M_z - M_0 \end{bmatrix} \quad (2.3)$$

where, M_0 is magnetization. M_x, M_y, and M_z are the components of magnetization. T_1 is spin–lattice relaxation time and T_2 is spin–lattice relaxation time.

During the rf pulse period ($2B1\cos\omega t$), the Bloch equation solution in the rotation coordinate is:

$$M'_x = 0$$

$$M'_y = M_0 \sin(\gamma B_1 t)$$

$$M'_z = M_0 \cos(\gamma B_1 t) \quad (2.4)$$

It means that during the rf pulse period, the magnetization is rotation in yz plane. This rotation can be tuned to any angle by applying a pulsed rf wave of an appropriate length. Fig.1-2 shows the net magnetization rotating 90^0 into the x, y plane by applying a pulse, called ($\frac{\pi}{2}$) pulse.

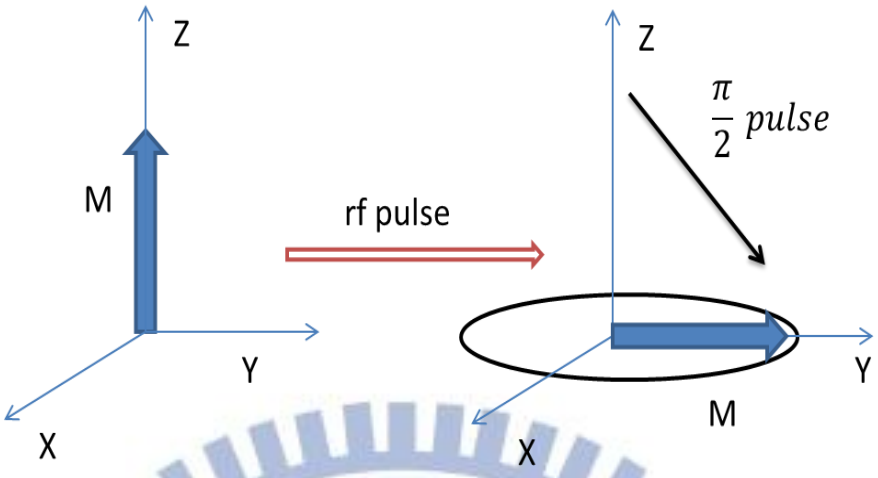

Fig.2-2 Magnetization rotated by rf pulse

After rf pulse, the Bloch equation solution is

$$M_x = M_0 sin\theta_0 \sin(\omega_0 t) e^{-\frac{t}{T_2}}$$

$$M_x = M_0 sin\theta_0 \cos(\omega_0 t) e^{-\frac{t}{T_2}}$$

$$M_z = M_0[1 + (cos\theta_0 - 1)e^{-\frac{t}{T_1}}] \quad (2.5)$$

This result is show that the magnetization motion is called precession. But the x and y component of the magnetization is decay by $e^{-\frac{t}{T_2}}$, at the same time, the magnetization is go back to the z-axis.

The precessing transverse magnetization will induced an oscillating voltage if the nuclei are inside a coil (Fig.2-3), but the oscillating voltage will decay because the magnetization is go back to the z-axis. This oscillating voltage gives the NMR signal. This oscillating voltage is called the NMR signal or free induction decay (FID). Note that the coil is perpendicular to the applied magnetic field in order to detect the precessing transverse magnetization.

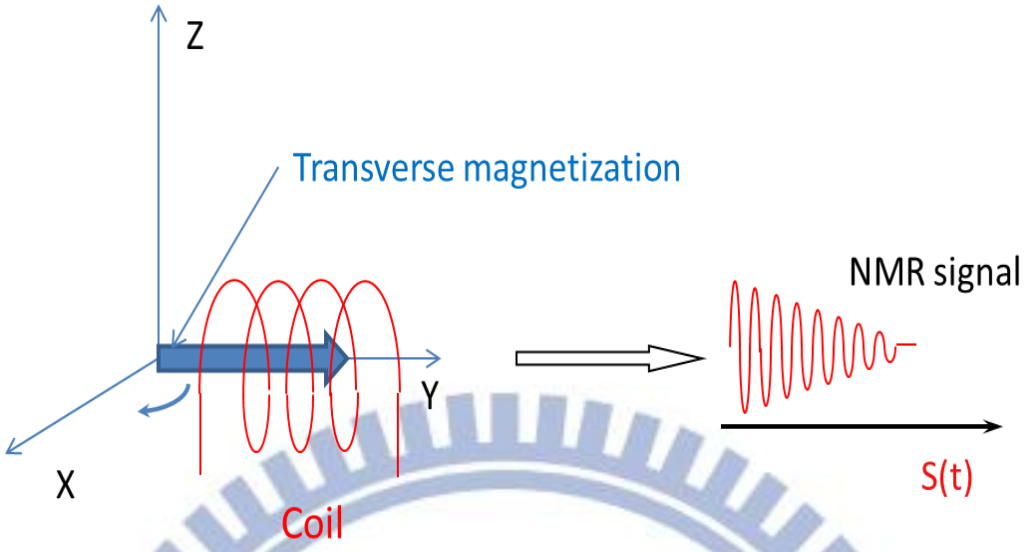

Fig2-3. The induction of an NMR signal.

The FID usually decays faster than the dead time of the rf pulse, which can make it undetectable. This problem may be solved by using the spin echo pulse sequences, as shown in Fig.2-4. The interval between the first and the second pulse is τ. The signal, called spin echo, appears at ~ 2τ after the first pulse. We can choose τ long enough to make the signal appear outside the dead time.

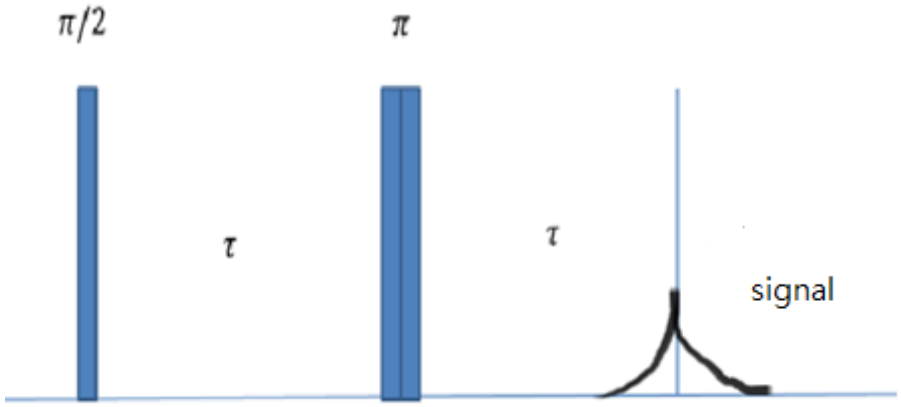

Fig.2-4 Spin echo pulse sequence.

2-**3** Frequency shift

According 2-1 and 2-2, the resonance frequency is related to external magnetic field and nucleus. But in the NMR experiment, there have a secondary magnetic field from the electrons and neighboring atoms. This secondary field contributes to the total field felt at the nucleus, and therefore has the potential to change the resonance frequency of the nucleus. Therefore, the resonance frequency is rewritten as

$$\omega' = \gamma(B_0 + \Delta B) = \gamma(1 + K)B_0 \quad (2.6)$$

The value of $\frac{\Delta B}{B_0}$ is defined as K (frequency shift). The NMR frequency shift is proportional to local susceptibility (χ).

The NMR frequency shift can have different origins and may be written as:

$$\mathrm{K} = K^{dia} + K^{orb} + K^{spin} \quad (2.7)$$

K^{dia}: The frequency shift is due to diamagnetic susceptibility.

K^{orb}: The frequency shift is due to the orbital part of the electronic susceptibility (χ^{orb}),which is usually temperature independent.

K^{spin}: The frequency shift is due to the local electronic spin susceptibility.

2-4 Electric Quadrupole Effect

For a spin I>1/2 nucleus, the nuclear charge distribution is not spherically symmetric (Fig.1-5) so that it can have a nuclear electric quadrupole moment. If the nucleus is located at a site with the crystal symmetry less than cubic, its quadrupolar moment would interact with the local electric field gradient (EFG).

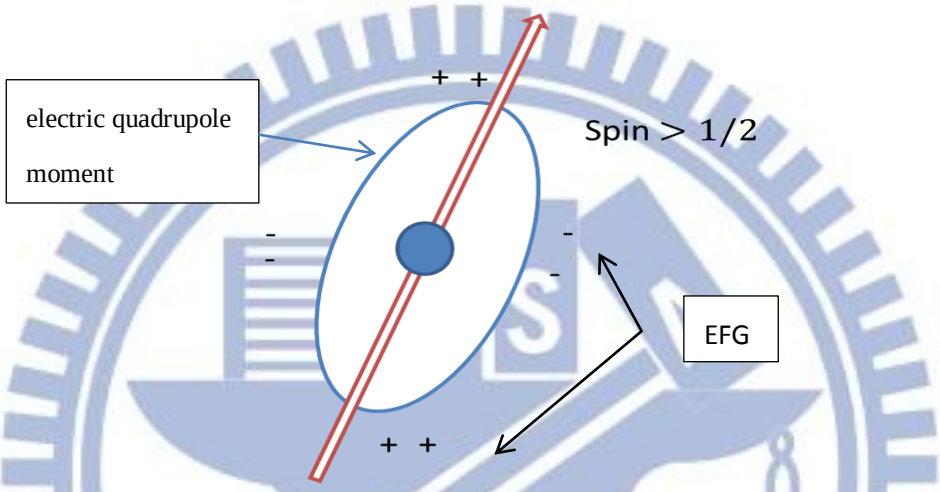

Fig.2-5 Electric charge distribution around the nuclei.

The Hamiltonian for the quadrupolar interaction can be written as

$$\widehat{H_Q} = \frac{eQ}{6I(2I-1)\hbar}\hat{I}\cdot e\boldsymbol{q}\cdot\hat{I} \quad (2.8)$$

where e**q** is the electric field gradient at the nucleus, $\hat{I}$ is the nuclear spin vector and eQ is the nuclear quadrupole moment.

If applying a magnetic field to the quadrupolar nucleus, the total Hamiltonian is H= H_z + H_Q, where Hz and HQ are the Hamiltonian for the Zeeman and quadrupolar interactions, respectively. If Hz>>HQ and the EFG has axial symmetry, the eigenvalues by the first order perturbation theory are [1]:

$$E_m = -\gamma\hbar B_0 m + \frac{e^2qQ}{4I(2I-I)}\left(\frac{3(\cos\theta)^2-1}{2}\right)[3m^2 - I(I+1)] \quad (2.9)$$

where, θ is the angle of the EFG direction between the applied magnetic field direction. The Fig.1-6 is the energy levels splitting for I=3/2.

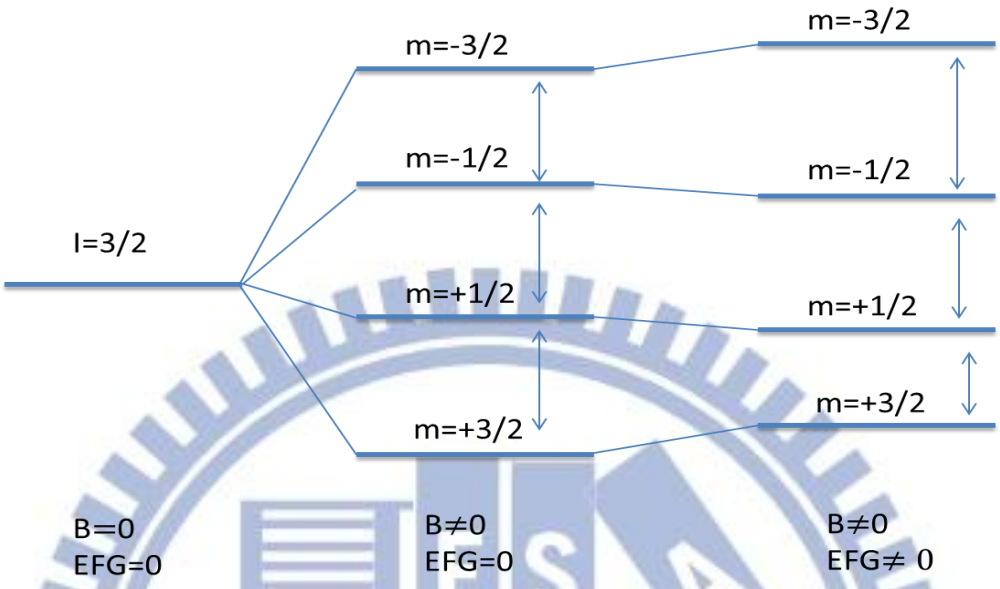

Fig.2-6 The nucleus with I=3/2 energy levels splitting in the applied magnetic field and EFG.

The energy levels are not equidistant so that the NMR spectrum has more than one peak, i.e., the central line and the satellite lines. For spin I=3/2, the resonance frequency of central line is $\omega = \omega_0 = \gamma B_0$, and the resonance frequency of satellite line are $\omega = \omega_0 \pm \omega_Q \frac{(3cos^2\theta - 1)}{2}$, where $\omega_Q = \frac{3e^2qQ}{2\hbar I(2I-I)}$ (Fig.2.10).

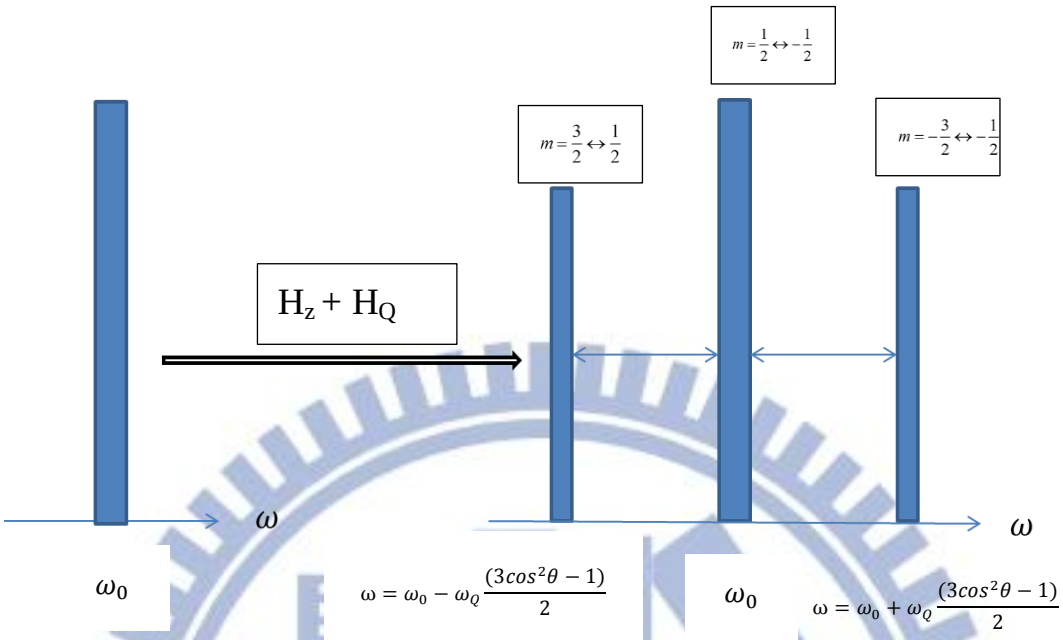

Fig.2-7 NMR spectrum for spin I=3/2 in quadrupole effect.

For a spin I>1 nucleus, the energy levels can split by the interaction of an electric quadrupole moment with an electric field gradient. The Fig.2-8 shows the nuclei (spin I=$\frac{3}{2}$) energy levels are split by an EFG.

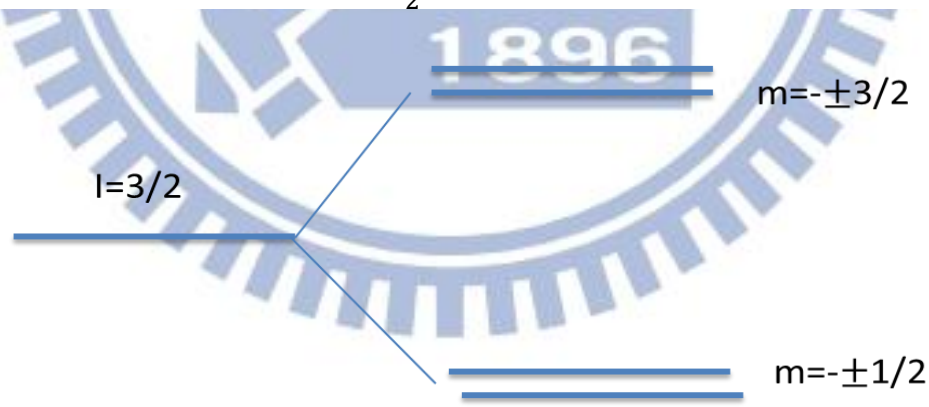

Fig.2-8 The energy levels are split by EFG.

2-5 Spin-lattice relaxation time

Spin-lattice relaxation is a process in which the z component of the magnetization (M_z) from the nonequilibrium state returning to the equilibrium states. It is characterized by the spin–lattice relaxation time T_1. The spin-lattice relaxation involves energy transfer where the nuclei release the energy (obtained from the RF pulse) to the surrounding lattice, thereby restore their equilibrium state. In fact, the energy exchange for this relaxation process can also occur in the hyperfine interaction or dipolar magnetic interaction.

The spin-lattice relaxation rate can be measured by a saturation recovery method. The pulse sequence is $\frac{\pi}{2} - \tau - \frac{\pi}{2} -$ signal. The first pulse is to saturate Mz, i.e., to make Mz=0. After the first pulse the M_z start to relax. The second pulse is used to measures the magnetization after the waiting period τ. The relaxation curve for the simplest case can be written as

$$M(\tau) = M_0(1 - e^{-\frac{\tau}{T_1}}) \quad (2.11)$$

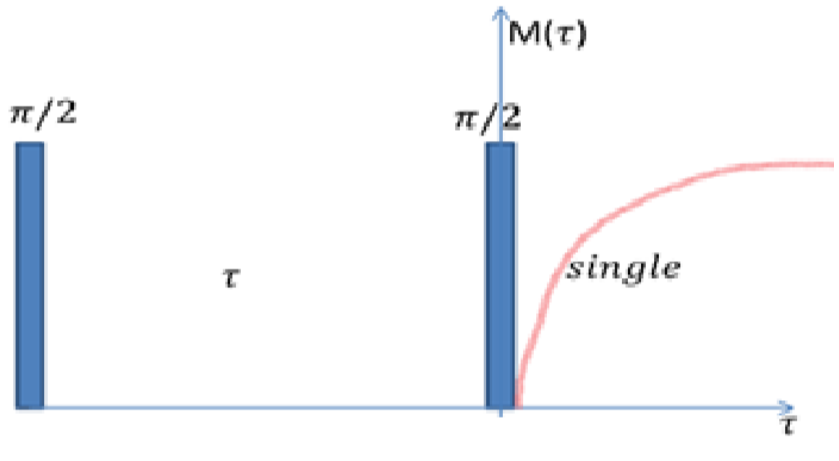

Fig.2-9 Pulse sequences for T_1 measurement and NMR single

2-6 Spin-Spin relaxation time

Spin-spin relaxation is a process in which the transverse components of the magnetization (M_{xy}) decays toward its equilibrium M_{xy}=0. It is characterized by the spin–spin relaxation time T_2. The magnetic dipole–dipole interaction leads to pairs of nuclei spins which exchange their polarization. This causes an exponential decay of the spin-echo intensity as a function of the time interval 2τ. Therefore, T_2 scales mainly with the strength of the interaction between neighbor nuclear spins.

The pulse sequence to measure the spin-spin relaxation time constant T_2 is $\frac{\pi}{2} - \tau - \pi - \tau -$ single, show in Fig.2-10. The M_{xy} after waiting for a time 2τ is given by

$$M(\tau) = M_0(e^{-\frac{t}{T_2}}) \quad (2.12)$$

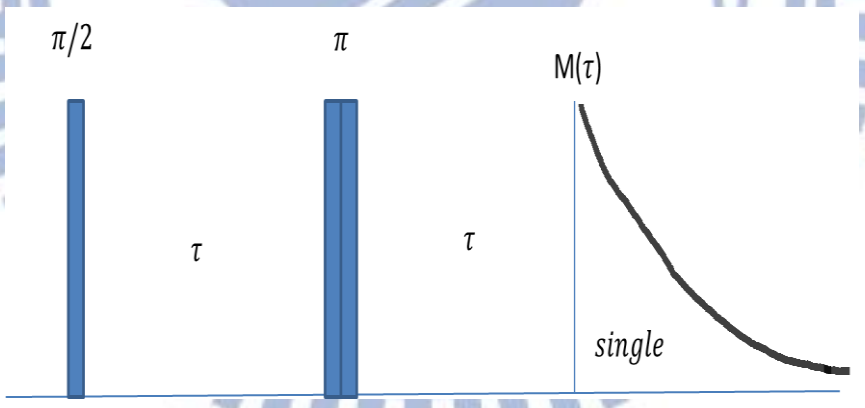

Fig2-10 Pulse sequences for T_2 measurement and NMR single

Chapter3 NMR example result and discuss

3-1 NMR study of $Bi_{2-x}Pb_xSr_zCo_2O_y$

In this chapter, we study the three different chemical compositions of $Bi_{2-x}Pb_xSr_zCo_2O_y$ single crystal (x=0-0.61, y=8.47-8.62, z=1.78-1.99). These three samples are making by F. C. Chou group (Center for Condensed Matter Sciences, National Taiwan University, Taiwan), and the chemical compositions is shown in table I. The magnetic susceptibility as a function of temperature for the each sample is shown in Fig.3-1. We found that the Pb-doped samples (sample B and C) have obvious larger temperature independent magnetic susceptibility than un-doped sample (sample A). So, we want to use NMR techniques to found out why the Pb-doped sample has higher temperature independent magnetic susceptibility than un-doped sample.

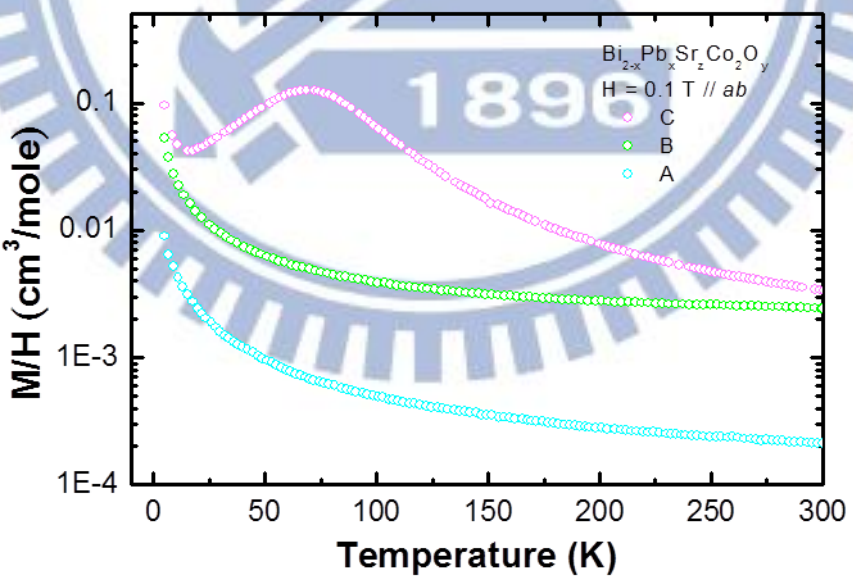

Fig.3-1 The temperature dependence magnetic susceptibility of three samples.

3-1-1 ^{59}Co NMR spectra

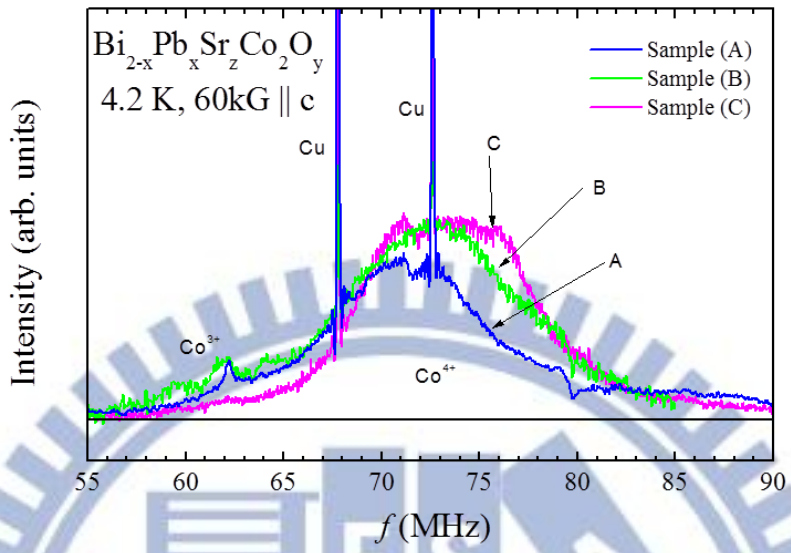

Fig.3-2 The ^{59}Co NMR spectra at 4.2K for sample A ,B and C with the magnetic field 60KG. The Cu peaks are from the NMR coils.

We measured ^{59}Co NMR spectra in the three different $Bi_{2-x}Pb_xSr_zCo_2O_y$ samples. In the Fig.3-2, we found that the ^{59}Co NMR spectra have two peaks (not the two very sharp single), which are representative two charge states of Co^{3+} and Co^{4+}. According to the previously study, spin state of Co^{3+} (S=0) and Co^{4+} (S=1/2) are in low spin state. [8-10]. The one with higher frequency and broad linewidth is from Co^{4+} site and the other with lower frequency and narrow linewidth is due to Co^{3+} site, because of their different magnetic shielding. The two very sharp single in Fig.3-2, which are from copper coils in NMR instrument. This copper coil is used by probe our sample. In addition, the Co^{4+} peak intensity in Pd-doped sample B and C is larger than un-doped sample A, suggesting that Pb doping enhances the concentration of Co^{4+}. We also found that the shape of Co^{4+} peak in sample A and B is symmetric, but is not symmetric in the sample C. It means that the sample C may have magnetic order.

Fig.3-3, Fig.3-4, and Fig3-5 show the ^{59}Co NMR spectra for sample A, B, and C at different temperature. We can see that the Co^{4+} peak will disappears when the temperature is above 50K, but the Co^{3+} peak still exist even temperature above 50K.

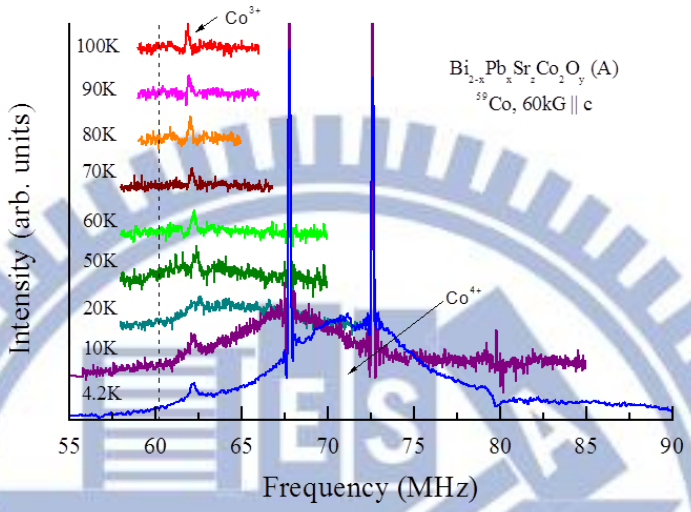

Fig.3-3 The ^{59}Co NMR spectra for sample A.

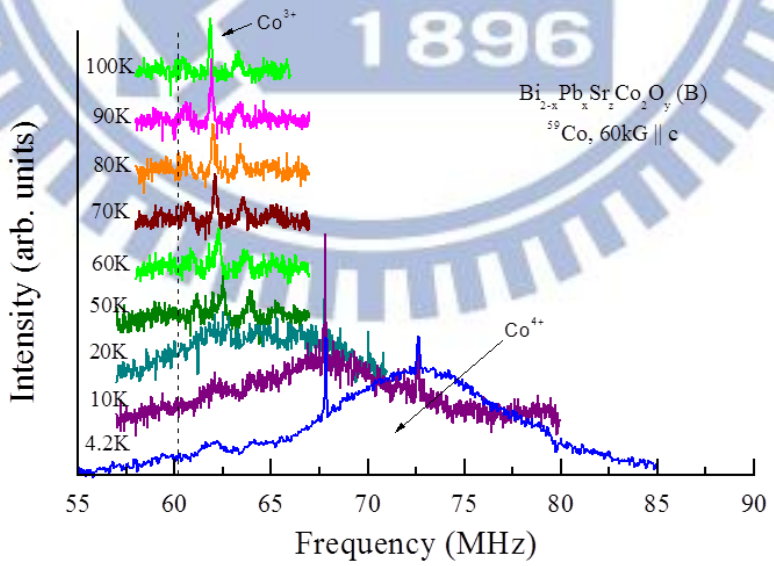

Fig.3-4 The ^{59}Co NMR spectra for sample B.

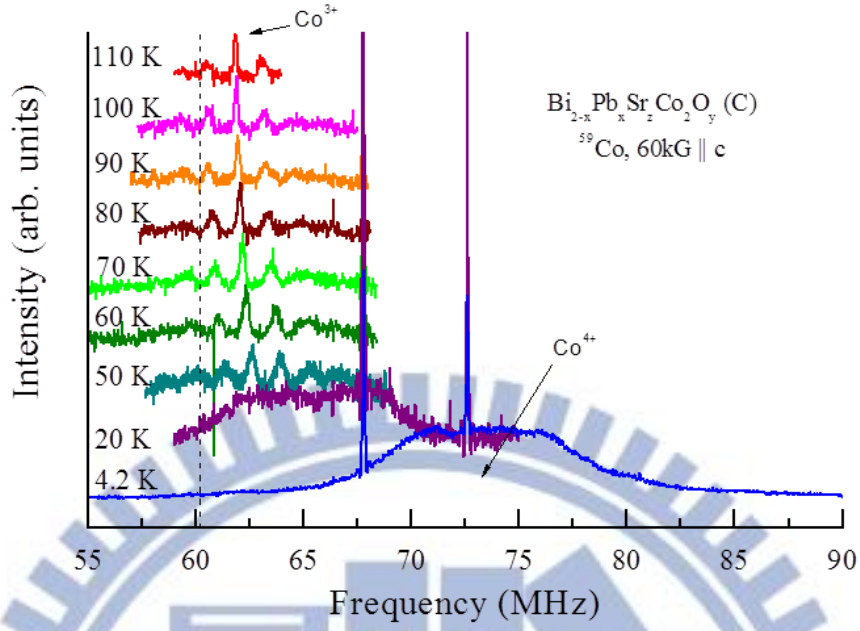

Fig.3-5 The ^{59}Co NMR spectra for sample C.

3-1-2 Frequency shift

The frequency shifts of the Co^{3+} site is show in Fig.2-8. We expect the Pb-doped samples have larger peak frequency shift than un-doped sample in high temperature region (T>100K). However, we don't found obvious difference in these three samples in Fig.3-8.

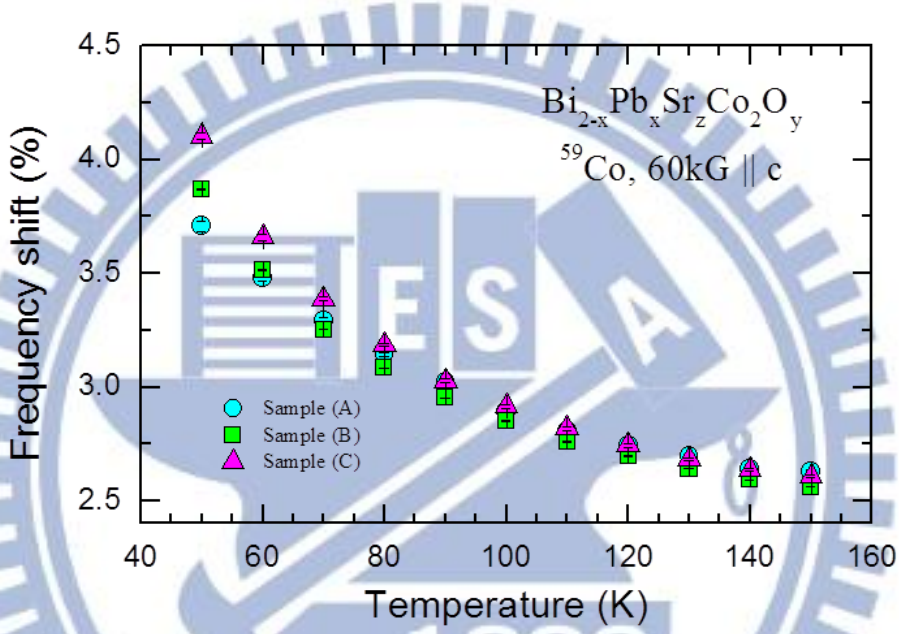

Fig.3-8 The Co^{3+} peak frequency shift as a function of temperature in sample A, B and C.

As we know, the NMR frequency shift can reflect the local magnetic susceptibility, and it can be expansion as:

$$K_{Co^{3+}}(\mathrm{T}) = \sum_{n,n} A_{hf,Co^{3+}}\chi_{d,Co^{4+}}(T) + A_{orb,Co^{3+}}\chi_{orb,Co^{3+}} + A_{Pauil,Co^{3+}}\chi_{Pauil} \quad (3\text{-}1)$$

where,

$\chi_{d,Co^{4+}}$: The spin susceptibility of Co^{4+} 3d electrons.

$\chi_{orb,Co^{3+}}$: The orbital susceptibility of Co^{3+} 3d electrons.

χ_{Pauil} : The Pauli susceptibility.

$A_{hf,Co^{3+}}$, $A_{orb,Co^{3+}}$, and $A_{Pauil,Co^{3+}}$: The hyperfine coupling constant with the $\chi_{d,Co^{4+}}$, $\chi_{orb,Co^{3+}}$, and χ_{Pauil}.

The first term in equation 3-1 is temperature dependent, and the last two terms is temperature independent. However, the Fig.3-8 shows the orbital susceptibility of Co^{3+} and the Pauli susceptibility in three samples are nearly unchanged, it is not conform to the bulk magnetic susceptibilities shown in Fig.3-1. So, we suspect that enhanced the bulk temperature independent susceptibility should originate from the local susceptibility of Co^{4+} site. It means that if we increase the concentration of Co^{4+}, the Co^{4+} orbital susceptibility also increase at the same time. This may explanation why it is not observed the peak frequency shift of Co^{3+} site and the Pb-dope samples have large temperature independent magnetic susceptibility. In addition, the frequency shifts of the Co^{3+} site have a little different in the low temperature region for three samples, suggesting that the Pb-doped samples have more Co^{4+} concentration.

3-2 NMR study of $(Bi_{0.25}Sb_{0.75})_2(Se_{2.35}Te_{0.65})$

Last year, our laboratory has been study the topological insulator Bi_2Se_3 by Zong-Yo Lai [21]. The example result shows ^{209}Bi NMR spectra anomaly, the center peak intensity is smaller than left and right sides peak. He thinks this phenomenon is due to each quadrupolar peak has different T_2 value. Since then, we want to know if we could still observe NMR spectra anomaly in the doped material $(Bi_{0.25}Sb_{0.75})_2(Se_{2.35}Te_{0.65})$, and study the atoms distribution inside the $(Bi_{0.25}Sb_{0.75})_2(Se_{2.35}Te_{0.65})$.

3-2-1 ^{209}Bi NMR spectra

We use two different repetition time (t_{rep}) to probe ^{209}Bi NMR spectra is show in Fig.3-12. In the different $t_{rep,}$ the spectra (A and B) do not change, it suggest that every point in the spectra has a similar T_1.

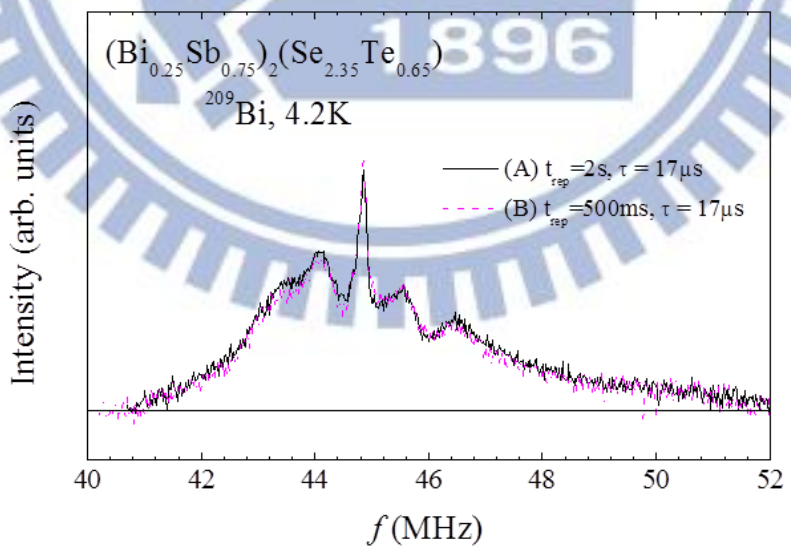

Fig.3-12 The ^{209}Bi NMR spectra with different repetition time (τ_{rep}).

In the Fig.3-13, the spectra A and B have different echo pulse spacing (τ). The spectra A is taken a short time interval τ = 17μs, so it involved the slow-relaxing and fast-relaxing Bi sites in the sample. The spectra B is from the slow-relaxing Bi sites with τ = 1.5ms. The signal of the fast-relaxing Bi sites (spectra C) could be obtained by subtraction of short τ (spectra A) and long τ (spectra B). According to above discuss, we can roughly separate Bi into two sites: the short spin-spin relaxation times T_2 type and long T_2 type, and the two T_2 type are represented the Bi atom bonding with Se atom and Te atom two sites.

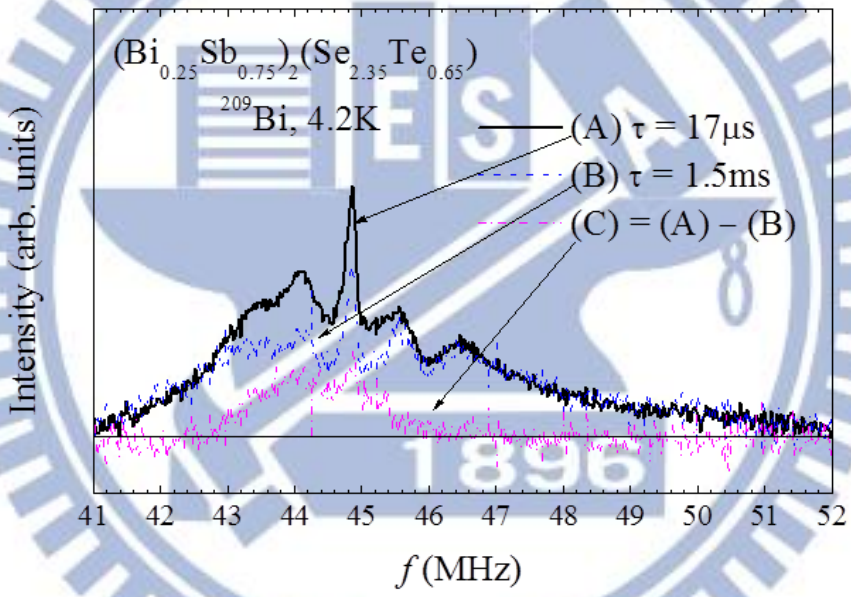

Fig.3-13 The spectra (A) is a short time intervalτ = 17μs, and The spectra (B) is a long time interval τ = 1.5ms.

3-2-2 Spin-spin relaxation time of ^{209}Bi

The spin-spin relaxation decay curve for ^{209}Bi atoms is shows in Fig.3-14. There have two T_2 components. This result is correspond with previous discuss. We also found the spin echo intensity is slightly modulated with time in Fig.3-15. This modulation in the T_2 relaxation curve is due to the quadrupolar interaction [26,27]. According to Ref.26, the period of the oscillation τ_m is related to the quadrouple splitting frequency ΔV_Q by the equation is:

$$\Delta \nu_Q \tau_m = 1 \quad (3\text{-}3)$$

From Fig.3-15, the modulation period τ_m is about 1.2μ sec, which corresponds to the quadrouple splitting frequency ΔV_Q is 0.83MHz.

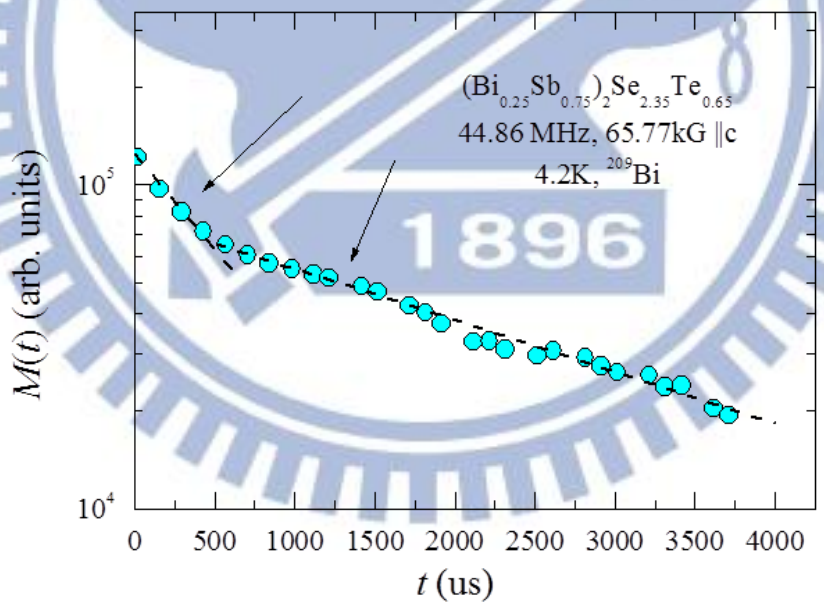

Fig.3-14 The spin-spin relaxation decay curve for Bi in 4.2K.

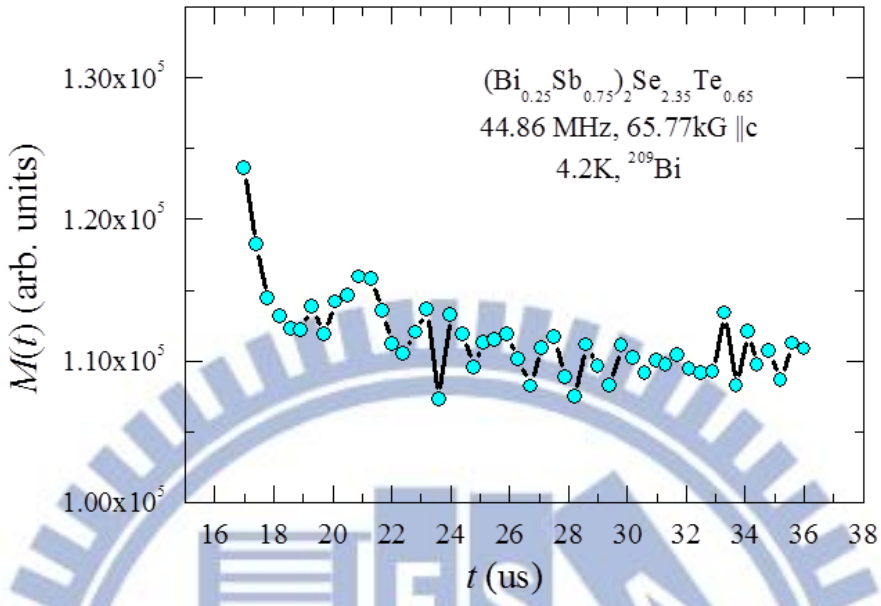

Fig.3-15 The modulation in the T_2 relaxation curve

3-2-3 ^{121}Sb NMR spectrum

The ^{121}Sb NMR spectrum measured is shown in Fig.3-16. The spectra change with τ, suggesting that Sb have different T_2 components. The spectra B is represent the slow-relaxing Sb sites and the spectra C is represent the fast-relaxing Sb sites. The spin-spin relaxation decay curve shows the two T_2 components in Fig.3-17, it means that the Sb atoms are bonding with Se and Te two atoms like Bi. The non-vanishing background signals suggest that the Sb sites experience a broad distribution of the local electric field gradient, and the broad spectra of Sb suggest that the substitution of Te and Sb is randomly distributed in the crystal.

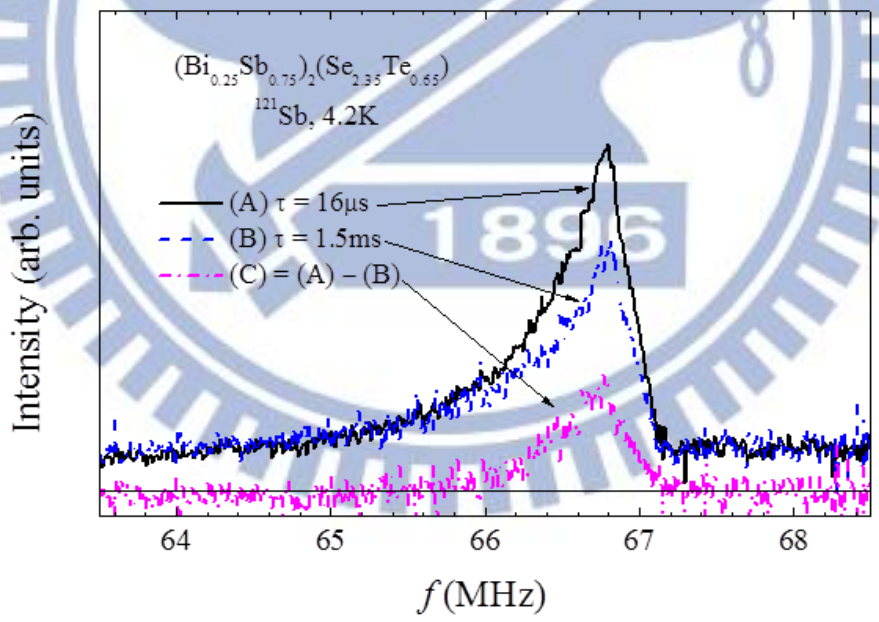

Fig.3-16 The spectra (A) is a short time interval τ = 16μs, and The spectra (B) is a long time interval τ = 1.5ms.

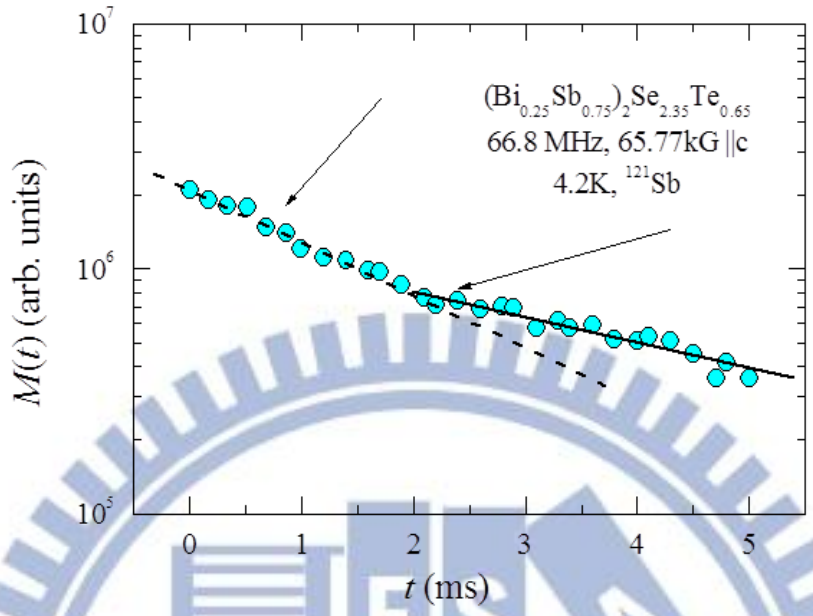

Fig.3-17 The spin-spin relaxation decay curve for Sb in 4.2K.

3-2-4 Temperature independent NMR spectra

We measured ^{209}Bi and ^{121}Sb NMR spectra in different temperature. The two atoms both show temperature independent NMR spectra (Fig.3-18, Fig3-19). It means that the NMR frequency shift can't reflect the weak temperature dependence magnetization.

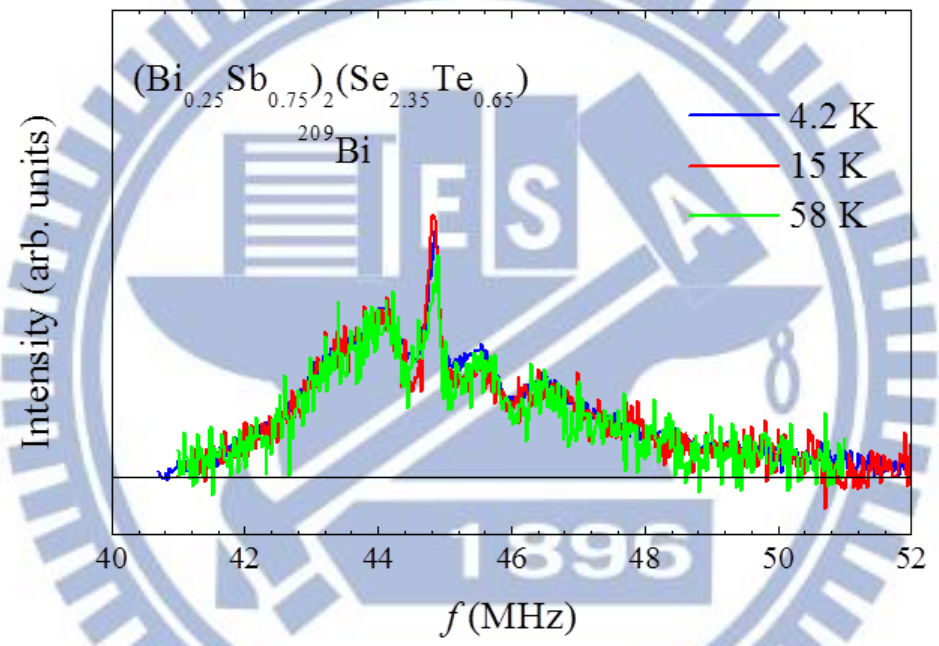

Fig.3-18 ^{209}Bi NMR spectra for different Temperature: 4.2K, 15K, and 58K.

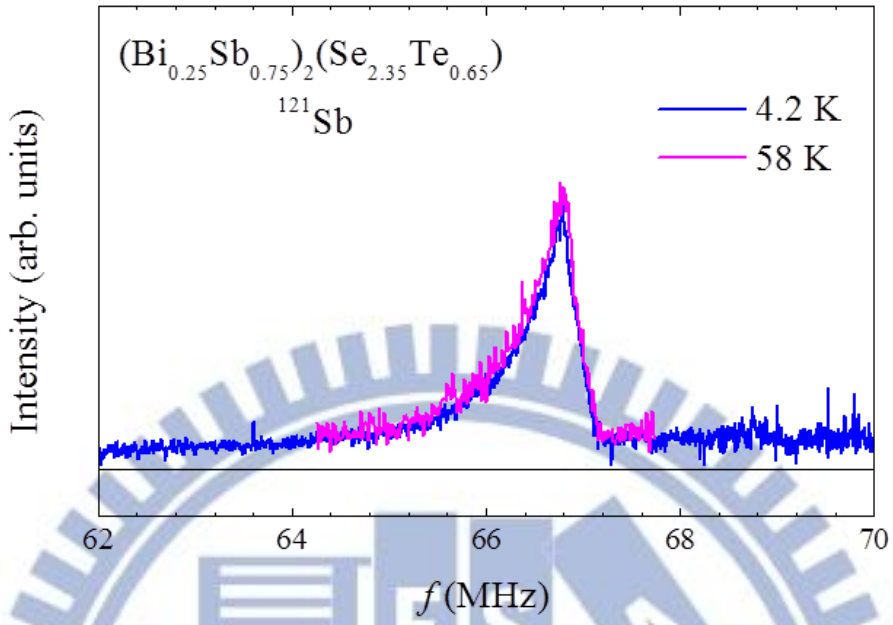

Fig.3-19 ^{121}Sb NMR spectra for different Temperature: 4.2K, 58K.

3-2-5 Spin lattice relaxation rate of ^{209}Bi and ^{121}Sb

The nuclear spin lattice relaxation rate ($1/T_1$) is a function of temperature is show in Fig.3-18. (logarithmic scale for the abscissas). We can separate two different slope of $1/T_1$ in ^{209}Bi and ^{121}Sb atoms. In the high temperature range, they have similarity slope. But in the low temperature range, the $1/T_1$ slope is quite different between the two atoms.

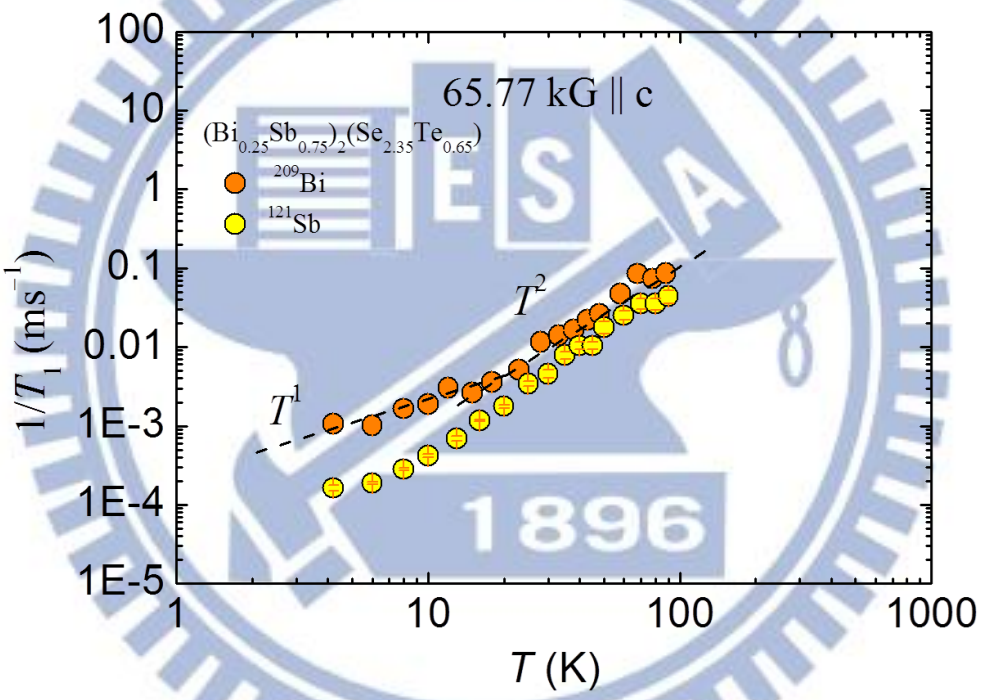

Fig.3-18 The spin lattice relaxation rate ($1/T_1$) for ^{209}Bi and ^{121}Sb.

The Fig.3-19 shows the $1/T_1$ ratio between the ^{209}Bi and ^{121}Sb, the uprising occurs at below 20 K, similar to the temperature where the susceptibility rises. This may suggest that they have the same reason. As we know the magnetic properties of the semiconductor may from electronic band structure. So we can say that in the low temperature

region, the electronic band structure is the main contribution to affect susceptibility and $1/T_1$ ratio. In the high temperature region, the $1/T_1$ ratio between the ^{209}Bi and ^{121}Sb are constant, it is because the $1/T_1$ ratio is contributed from lattice vibrate in high temperature.

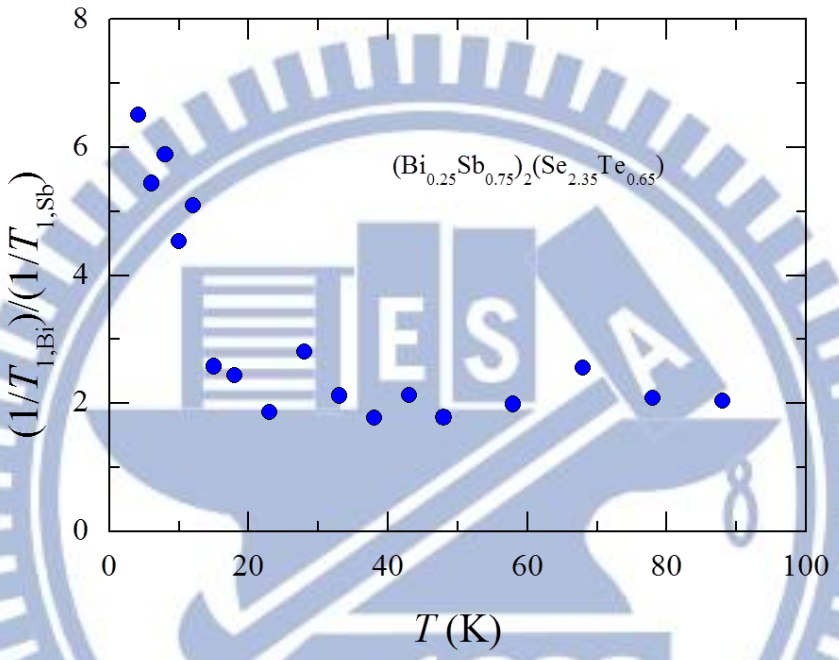

Fig.3-19 $1/T_1$ rate between the ^{209}Bi and ^{121}Sb.

3-2-6 Compare the Bi_2Se_3 and $(Bi_{0.25}Sb_{0.75})_2(Se_{2.35}Te_{0.65})$.

The ^{209}Bi NMR spectra in $(Bi_{0.25}Sb_{0.75})_2(Se_{2.35}Te_{0.65})$ and Bi_2Se_3 is show in Fig.3-20, the spectra anomaly disappears after chemical substitution. The linewidth of $(Bi_{0.25}Sb_{0.75})_2(Se_{2.35}Te_{0.65})$ is extraordinary broader than that of the Bi_2Se_3, this is suggest that Bi atoms are randomly distributed in the crystal. In addition, the nuclear quadrupolar splitting of $(Bi_{0.25}Sb_{0.75})_2(Se_{2.35}Te_{0.65})$ is larger than that of Bi_2Se_3, due to the strong lattice distortion by doping. We also found that the Bi_2Se_3 shows positive frequency shift, but the $(Bi_{0.25}Sb_{0.75})_2(Se_{2.35}Te_{0.65})$ shows negative frequency shift. Why they have different frequency shift? We can see that the $(Bi_{0.25}Sb_{0.75})_2(Se_{2.35}Te_{0.65})$ is more diamagnetic than Bi_2Se_3 in Fig.3-21, so the negative frequency shift is due to diamagnetic. But the positive frequency shift of Bi_2Se_3 is due to the Pauli susceptibility.

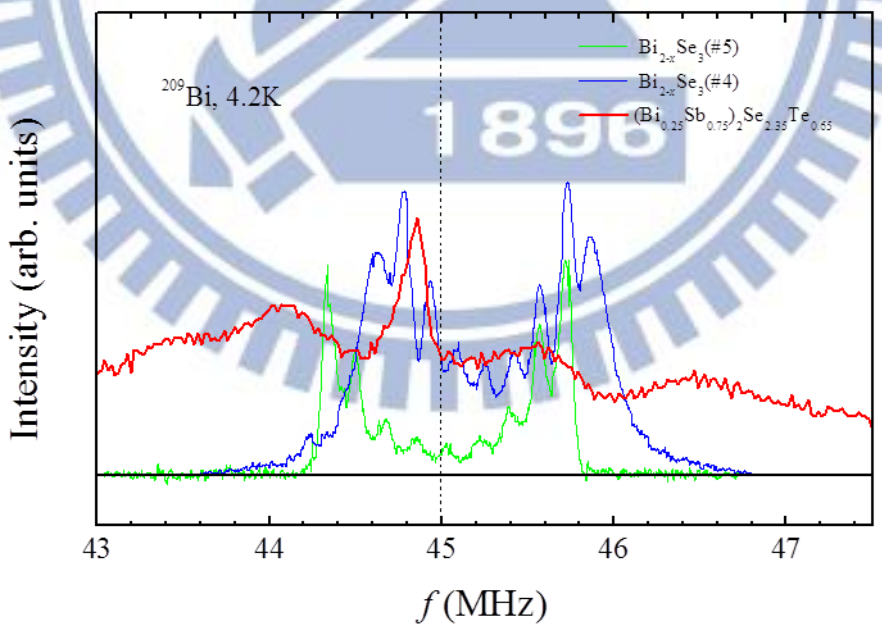

Fig.3-20 ^{209}Bi NMR spectra in Bi_2Se_3 and $(Bi_{0.25}Sb_{0.75})_2(Se_{2.35}Te_{0.65})$

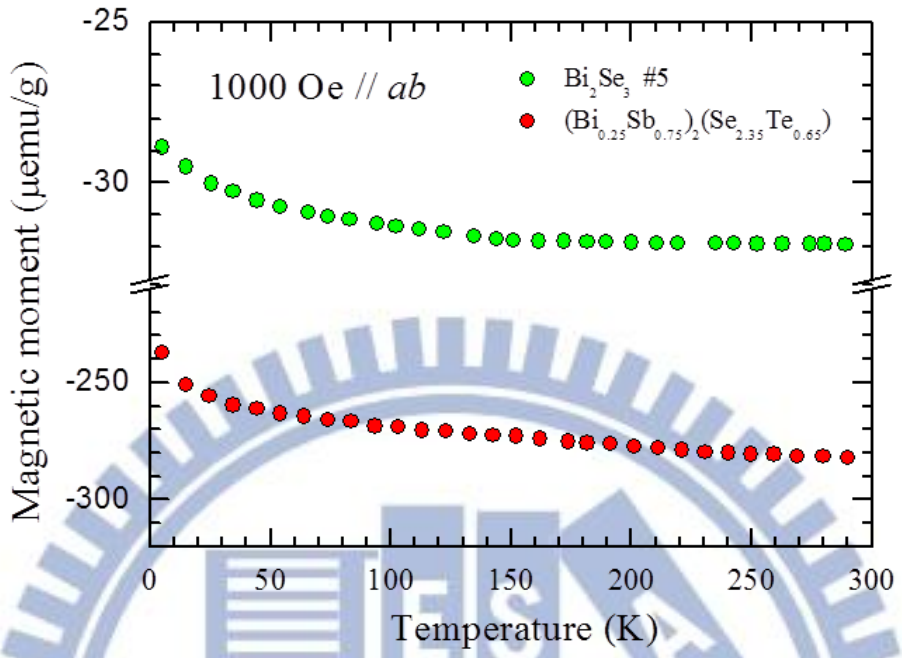

Fig.3-21 Magnetization of Bi_2Se_3 and $(Bi_{0.25}Sb_{0.75})_2(Se_{2.35}Te_{0.65})$.

Chapter 4 Conclusion

We used the NMR technique to study the doping effect of the $Bi_{2-x}Pb_xSr_zCo_2O_y$, which the Pb-doped sample have larger temperature independent magnetic susceptibility than un-doped sample. The frequency shift of Co^{3+} site in Fig.3-8, suggests that the enhanced temperature independent magnetic susceptibility is due to the orbital susceptibility of Co^{4+}. Therefore, we can understand that the larger temperature independent magnetic susceptibility in Pb-doped samples is because the Pb-doped samples have larger Co^{4+} concentration.

Next, we study the topological insulator $(Bi_{0.25}Sb_{0.75})_2(Se_{2.35}Te_{0.65})$. We measured ^{209}Bi and ^{121}Sb NMR spectra, spin-spin relaxation time, and spin-lattice relaxation time. The broad spectra of ^{209}Bi and ^{121}Sb suggest that the substitution of Te and Sb is randomly distributed in the crystal. Both ^{209}Bi and ^{121}Sb spectrum could be separated into the slow and fast T_2 components, it means that they are bonding with Se and Te two atoms. In addition, the nuclear quadrupolar splitting of $(Bi_{0.25}Sb_{0.75})_2(Se_{2.35}Te_{0.65})$ is larger than that of Bi_2Se_3 is because of the strong lattice distortion by doping. Finally, the spin lattice relaxation rate of ^{209}Bi and ^{121}Sb are telling us the weak temperature dependence susceptibility is related to the temperature dependent band parameters. Summary, the NMR result shows the $(Bi_{0.25}Sb_{0.75})_2(Se_{2.35}Te_{0.65})$ has the strong lattice distortion, but the surface states still can existence in this material. This fact tell us the topological insulator surface state is not vanish by lattice distortion as long as not breaking the time reversal symmetry.

Chpater5 Appendix: Building an AC susceptometer

5-1 Introduction

The ac susceptometer is an important tool for characterizing many magnetic properties of materials. Because it is can measurement the magnetization dynamics which are not obtained in dc magnetic measurements. Therefore, the ac susceptometer offers the opportunity to study the magnetic susceptibility as a function of frequency and temperature. The main concept of ac susceptibility is the magnetization of the sample is changing to response an applied ac filed [28], and ac susceptometer design is based on the mutual inductance method [29].

5-2 Theoretical background

AC susceptibility is the magnetization of the sample follows the applied ac field either in-phase or with some phase lag. Therefore, we use the ac inductive method to measurement ac susceptibility [30-32]. For the ac susceptometer described below, we will give some information about ac susceptibility in this section.

The susceptibility is defined as

$$\chi = \frac{M}{H} \quad (5.1)$$

where, χ is the magnetic susceptibility, M is volume magnetization, and H is magnetic field.

Consider a sample in the applied ac magnetic field $\mathrm{H(t)} = H_0 \cos(\omega t)$, but the magnetic field in the sample will show a phase different θ behind an applied ac magnetic field. So the magnetization is

$$M = \chi H = \chi H_0 \cos(\omega t - \theta)$$

$$= \chi H_{ac}(cos\omega t cos\theta + sin\omega t sin\theta) \quad (5.2)$$

Define the complex AC susceptibility

$$\chi' = \chi \cos\theta$$

$$\chi'' = \chi \sin\theta \quad (5.3)$$

The physical meaning of χ' is: the time average of the magnetic energy stored in the volume occupied by the sample [31] is

$$W_m = \chi' \frac{B_a^2}{2\mu_0} \quad (5.4)$$

The physical meaning of χ'' is: The energy converted into heat during one cycle of the ac field [31] is

$$W_q = -2\pi\chi'' \frac{B_a^2}{2\mu_0} \quad (5.5)$$

As we have seen, both parts of the complex ac susceptibility characterize the energy exchange between the sample and the applied ac magnetic field. The χ' reflects the screening properties expressed as a difference between the energy in the normal state and the superconducting state. The χ'' corresponds to the amount of ac magnetic field energy converted to heat[28].

5-3 AC Susceptometer Design

The ac susceptometer typically consists of primary coil, pick-up coils, lock-in amplifier, and sample holder, and a typical circuit is shown in Fig.5-1(a). The ac suceptometer probe illustrated in Fig.5-1(b), includes a primary solenoid coil which produces an ac magnetic field. Inside the primary coil are the two pick-up coils which are wound in opposite

directions and electrically connected in series. The sample is placed in one of the pickup coils while the other pickup coil is left empty.

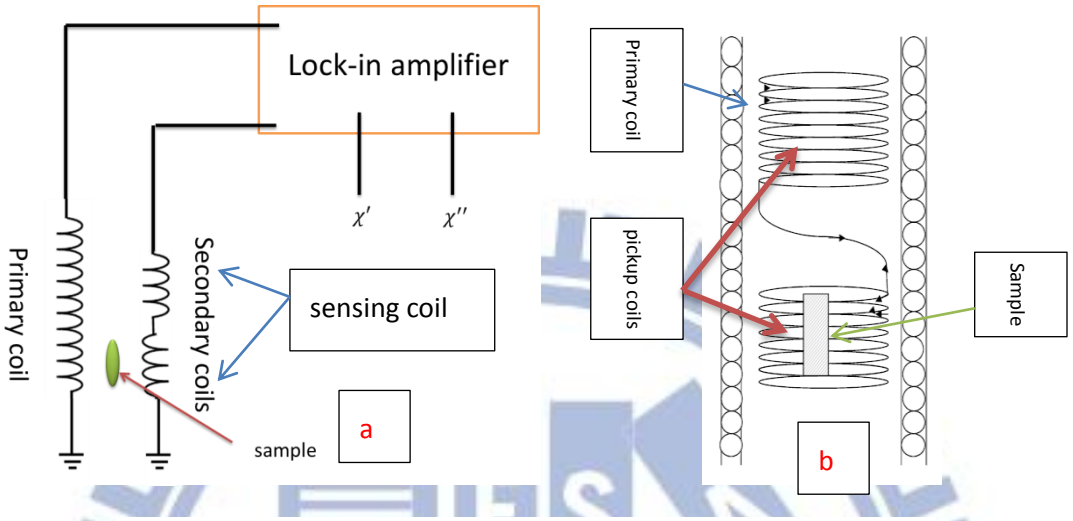

Fig. 5-1 (a)Experimental setup of the ac susceptometer

(b) AC suceptometer probe illustrated [32]

The magnetic flux through the N turn pick-up coil of radius a (see Fig.5-1) is [32]

$$\phi(t) = \pi a^2 N M(t) \mu_0 \quad (5.6)$$

The induced voltage V(t) across the pick-up coils is:

$$V(t) = -\frac{d\phi(t)}{dt} = -\pi a^2 N \mu_0 \frac{dM(t)}{dt}$$

$$= V_0 \chi(\cos\omega t\cos\theta - \sin\omega t\sin\theta)$$

$$= V_0(\chi' \cos\omega t - \chi'' \sin\omega t) \quad (5.7)$$

where $V_0 = \pi a^2 N \mu_0 \omega H_0$, here is a lock-in amplifier measurement voltage (see Fig.5-1).

The pick-up coils are connected to the differential input of a computer controlled lock-in amplifier (model SR830), and the lock-in amplifier measured voltage V_s is:

$$V_s(t) = V_x cos\omega t + V_y sin\omega t \quad (5.8)$$

Since $V_s(t)=V_0(t)$, where

$$V_x = V_0\chi'$$

$$V_y = -V_0\chi'' \quad (5.9)$$

The lock-in amplifier can direct measures of V_x and V_y.

The Fig.5-3 shows the dimensions of primary coil, pick-up coils, and sample holder. The pick-up coils are inserted into the primary coil and the sample holder is inserted into the lower pick-up coil.

Primary Coil
Wire gauge: 38(AWG)
Total number of turns: 1500
Units: mm

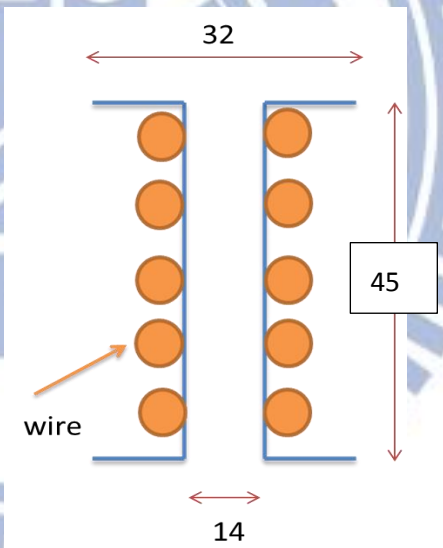

(a)

Secondary Coil
Wire gauge: 42(AWG)
Total number of turns: 420
Units: mm

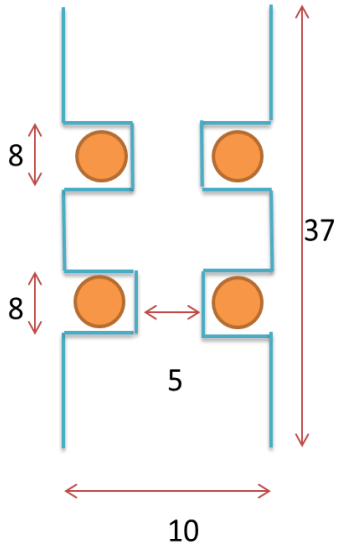

(b)

Sample holder
Units: mm

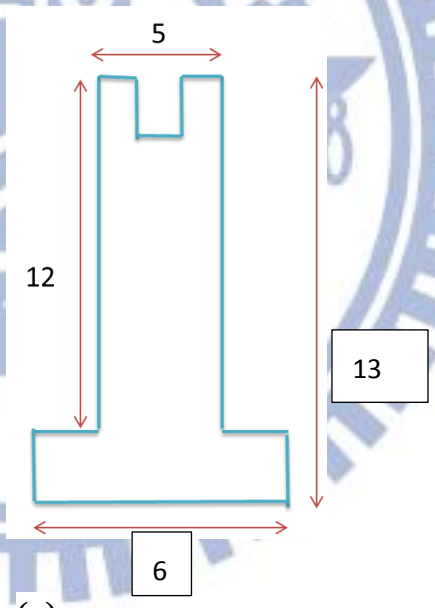

(c)

Fig.5-3 (a) Primary coil, (b) pick-up coils, and (c) sample holder geometry

5-4 Magnetic field and Calibration coefficient

The magnetic field inside the primary coil is use the long solenoid approximation to obtains:

$$B = \frac{\mu_0 NI}{l} \quad (5.10)$$

μ_0 is the permeability of free space, N is the number of turns, I is the current, and l is length of the solenoid.

The first step is found the current in the primary coil but we use the fix voltage generator to be our ac field source. So we have to obtain the total impedance first

$$Z = \sqrt{R^2 + (\omega L)^2} \quad (5.11)$$

here R is the resistance, L is the self-inductance of the coil, and ω is the angular frequency of the ac field. The self-inductance L can estimate by long coil approximation:

$$L = \frac{\mu_0 N^2 A}{l} \quad (5.12)$$

Then use the relationship $I = \frac{V}{Z}$ to estimate the current. Finally we can get the magnetic field by equation (5.10).

The signal from the pick-up coils is proportional to the susceptibility of the sample, and depends on experimental parameters. We get their relationship is [30]

$$V = \frac{1}{\alpha} H_a f V_s \chi_{ext} \quad (5.13)$$

where V is the measured voltage (units V), α is the calibration constant of the susceptometer (units $A.m^2.V^{-1}.s^{-1}$), V_s is the sample volume (units

m^3), f is the frequency of ac field (units s^{-1}), H_a is the magnetic field (units $A.m^{-1}$), and χ_{ext} is the susceptibility of the sample in SI units (dimensionless).

The calibration constant α is related between the sample shape and the secondary coil. We can expression the calibration constant α in the special case, when samples shape is spherical and secondary coils shape are long and thin [31].

$$\alpha = \frac{[\left(\frac{1}{2}L^2\right)+a^2]^{1/2}}{N_s \pi \mu_0} \quad (5.14)$$

where the parameters are the radius a, length L, and Ns turns of the secondary coils.

In our instrument, the α is:

$$\alpha = \frac{[(0.008)^2 + (0.0025)^2]^{1/2}}{420 \times \pi \times 4 \times \pi \times 10^{-7}} \simeq 5$$

5-5 AC susceptometer testing

We used the bulk superconducting sample YBCO to test our instrument. The applied ac magnetic field B is about 0.29Oe, and frequency is 1KHz. The Fig.5-5 and Fig.5-6 show the χ' and χ'' versus temperature measured. The blue point is representation the sample holder with sample, and the read point is meaning the sample holder without sample. We can see that our homemade ac susceptometer is able to work, and transition temperature for YBCO is about 97K. In this chapter, we reported the principle and geometry of ac susceptometer. And finally, it is shown our homemade ac susceptometer is could be work.

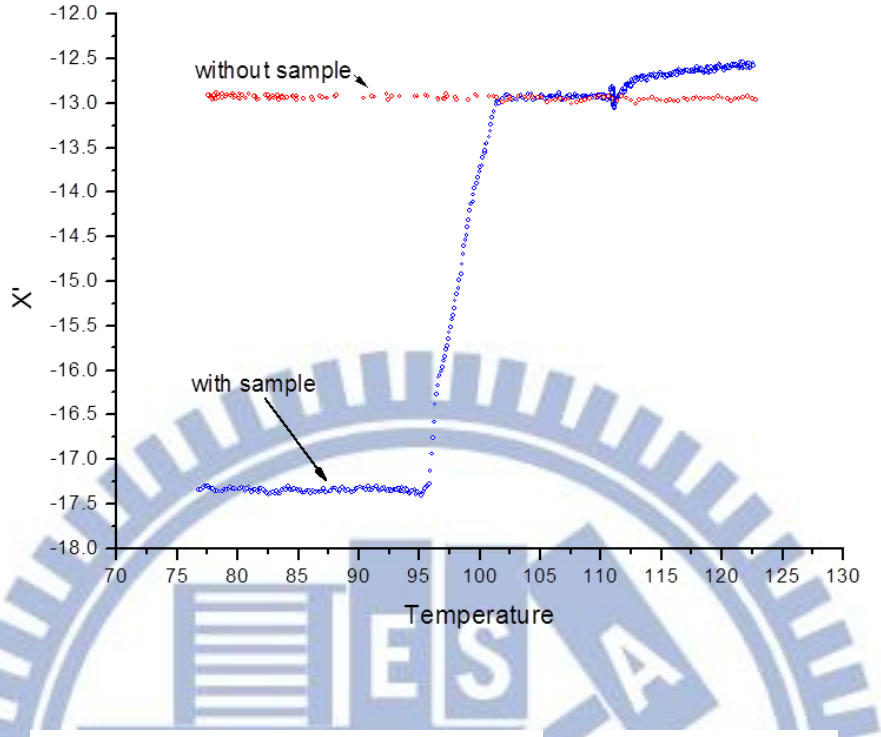

Fig.5-5 Real part of susceptibility (χ') vs temperature.

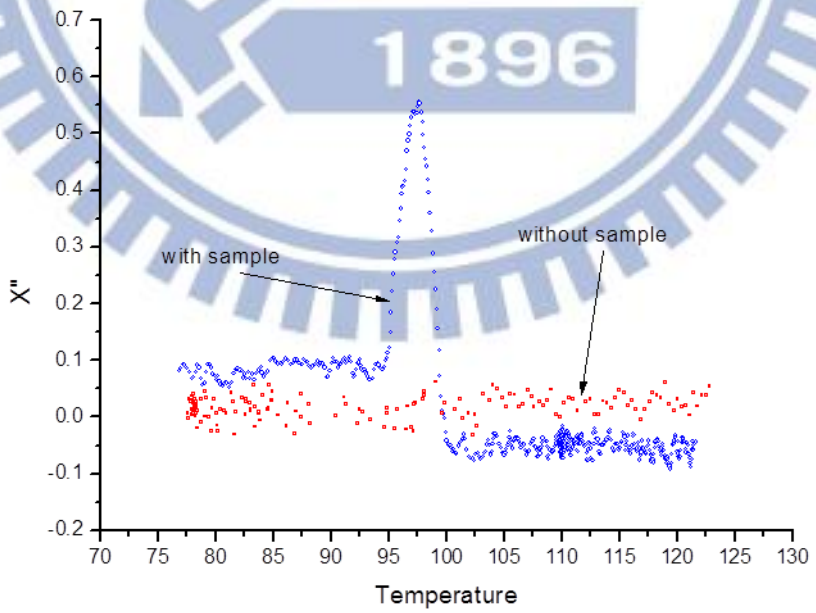

Fig.5-6 Imaginary part of susceptibility (χ'') vs temperature.

Reference

[1] I. Terasaki, Y. Sasago and K. Uchinokura, Large thermoelectric power in NaCo2O4 single crystals, Phys. Rev. B 56, R12 685 (1997).

[2] A. C. Masset, C. Michel, A. Maignan, M. Hervieu, O. Toulemonde, F. Studer, B. Raveau, and J. Hejtmanek, Misfit-layered cobaltite with an anisotropic giant magnetoresistance: $Ca_3Co_4O_9$, Phys. Rev. B 62 166 (2000).

[3] R. Funahashi, I. Matsubara, and S. Sodeoka, Thermoelectric properties of Bi2Sr2Co2Ox polycrystalline materials Appl. Phys. Lett. 76, 2385 (2000).

[4] R. Funahashia and M. Shikano, Bi2Sr2Co2Oy whiskers with high thermoelectric figure of merit, Appl. Phys. Lett 81, 1459 (2002).

[5] K. Takada, H. Sakurai, E. T. Muromachi, F. Izumi, R. A. Dilanian, and T. Sasaki, Superconductivity in two-dimensional CoO_2layers, Nature (London) 422, 53 (2003).

[6] T. Motohashi, R. Ueda, E. Naujalis, T. Tojo, I. Terasaki, T. Atake, M. Karppinen, and H. Yamauchi1, Unconventional magnetic transition and transport behavior in Na0.75CoO2, Phys. Rev. B67, 064406 (2003).

[7] I. Tsukada ,T. Yamamoto, M. Takagi, T.Tsubone, S. Konno, and K. Uchinokura, Ferromagnetism and Large Negative Magnetoresistance in Pb Doped Bi–Sr–Co–O Misfit-Layer Compound, J. Phys. Soc. Jpn. 70, 834 (2001).

[8] I. M. Sutjahja, The Change in Physical Properties of $Bi_2Ca_2Co_2O_8$ Thermoelectric Materials Induced by Pb and Rare-Earth Dopings, IJP Vol. 22 No. 3 (2011).

[9] T. Mizokawa, L. H. Tjeng, P. G. Steeneken, N. B. Brookes, I. Tsukada, T.Yamamoto, and K. Uchinokura, Photoemission and x–ray -absorption study of misfit-layered (Bi,Pb)-Sr-Co-O compounds: Electronic structure of a hole-doped Co-O triangular lattice, Phys. Rev. B. 64, 115104 (2001).

[10] W. Koshibae, K. Tsutsui, and S. Maekawa, Thermopower in cobalt oxides, Phys. Rev. B. 62, 6869 (2000).

[11] T. Yamamoto, K. Uchinokura, and I. Tsukada, Physical properties of the misfit-layered (Bi,Pb)-Sr-Co-O system:Effect of hole doping into a triangular lattice formed by low-spin Co ions, Phys. Rev. B. 65, 184434 (2002).

[12] W. Koshibae and S. Maekawa, Effects of Spin and Orbital Degeneracy on the Thermopower of Strongly Correlated Systems, Phys. Rev.Lett. 87, 236603 (2001).

[13] H. Leligny, D. Grebille, O.PeÂ rez, A. C. Masset, M. Hervieu, and B.Raveau, A five-dimensional structural investigation of the misfit layer compound [Bi0.87SrO2]2[CoO2]1.82, C. R. Acad. Sci. Paris, Serie II 2 409 (1999).

[14] M. Z. Hasan, C. L. kane, Colloquium: topological insulators, Rev. Mod. Phys. 82, 3045–3067 (2010).

[15] X. L. Qi, and S. C. Zhang, Topological insulators and superconductors, Rev. Mod. Phys. 83, 1057–1110 (2011).

[16] Y. L. Chan, et al. Science 329, 659 (2010).

[17] D. Hsieh, D. Qian, L. Wray, Y. Xia, Y. S. Hor, R. J. Cava, and M. Z. Hasan, A topological Dirac insulator in a quantum spin Hall phase, Nature 452, 970-974 (2008).

[18] K. Zhang, C. X. Liu, X. L. Qi, X. Dai, Z. Fang and S. C. Zhang, Topological insulators in Bi2Se3, Bi2Te3 and Sb2Te3 with a single Dirac cone on the surface, Nature 5, 438 - 442 (2009)

[19] Y. L. Chen, J. H. Chu, J. G. Analytis, Z. K. Liu[1,2], K. Igarashi, H.-H. Kuo, X. L. Qi, S. K. Mo, R. G. Moore, D. H. Lu, M. Hashimoto, T. Sasagawa, S. C. Zhang, I. R. Fisher, Z. Hussain and Z. X. Shen, Massive Dirac Fermion on the Surface of a Magnetically Doped Topological Insulator, Science 329, 659 (2010).

[20] D. Hsieh, Y. Xia, D. Qian, L. Wray, J. H. Dil, F. Meier, J. Osterwalder, L. Patthey, J. G. Checkelsky, N. P. Ong, A. V. Fedorov, H. Lin, A. Bansil, D. Grauer, Y. S. Hor, R. J. Cava, and M. Z. Hasan, A tunable topological insulator in the spin helical Dirac transport regime, Nature 460, 1101-1105 (2009)

[21] 賴宗佑，拓譜絕緣體 Bi_2Se_3 的核磁共振研究，國立交通大學電子物理學系碩士論文 (2011)

[22] D. Vasilevskiy, P. Fréchette, S. Turenne, and R.A. Masut, Thermoelectric properties and transport phenomena in $(Bi_{1-x}Sb_x)_2(Te_{1-y}Se_y)_3$ quaternary n-type alloys produced by powder metallurgy and extrusion, IEEE 05, 0-7803-9552-2 (2005)

[23] Lei Jia, Peng Hu, Zeshao Chen, and Wei Sun, International Journal of Thermophysics, Vol. 27, No. 1 (2006)

[24] A. A. Taskin, Zhi Ren, Satoshi Sasaki, Kouji Segawa, and Yoichi Ando, Observation of Dirac Holes and Electrons in a Topological Insulator, Phys. Rev. Latt. 107, 016801 (2011)

[25] Zhi Ren, A. A. Taskin, Satoshi Sasaki, Kouji Segawa, and Yoichi Ando, Optimizing $Bi_{2-x}Sb_xTe_{3-y}Se_y$ solid solutions to approach the

intrinsic topological insulator regime, Phys. Rev. B 84, 165311 (2011)

[26] Hisashi ABE, Hiroshi YASUOKA, and Akira HIRAI, Spin Echo Modulation Caused by the Quadrupole Interaction and Multiple Spin Echoes, JPESJ, 21, 77 (1966)

[27] D. Fekete, H. Boasson, A. Grayevski, V. Zevin, and N. Kaplan, Anisotropic hyperfine interactions in ferromagnetic hcp Co, Phys. Rev. B 17,347 (1978)

[28] R. A. Hein, T. L. Francavilla, and D. H. Liebenberg, *Magnetic Susceptibility of Superconductors and Other Spin Systems*, Springer, (1991)

[29] R. B. Goldfarb and J. V. Minervini, Calibration of ac susceptometer for cylindrical specimens, Rev. Sci. Instrum. 55, 5 (1984)

[30] F. Gomory, Characterization of high temperature superconductors by AC susceptibility measurements, Supercond. Sci. Technol. 10 523–542 (1997).

[31] M. I. Youssif, A. A. Bahgat, and I. A. Ali, AC Magnetic Susceptibility Technique for the Characterization of High Temperature Superconductors, Egypt. J. Sol., 23, 2, (2000)

[32] M. Nikolo, Superconductivity: A guide to alternating current susceptibility measurements and alternating current susceptometer desidn, Am. J. Phys. 63, 1 (1995)